Gravitational waves and mass ejecta from binary neutron star mergers: Effect of the stars' rotation

Tim Dietrich[1], Sebastiano Bernuzzi[2], Maximiliano Ujevic[3], and Wolfgang Tichy[4]
[1]*Max Planck Institute for Gravitational Physics, Albert Einstein Institute, D-14476 Golm, Germany*
[2] *DiFeST, University of Parma, and INFN Parma I-43124 Parma, Italy*
[3]*Centro de Ciências Naturais e Humanas, Universidade Federal do ABC, 09210-170, Santo André, São Paulo, Brazil and*
[4] *Department of Physics, Florida Atlantic University, Boca Raton, FL 33431 USA*
(Dated: November 23, 2016)

We present new (3+1) dimensional numerical relativity simulations of the binary neutron star (BNS) mergers that take into account the NS spins. We consider different spin configurations, aligned or antialigned to the orbital angular momentum, for equal and unequal mass BNS and for two equations of state. All the simulations employ quasiequilibrium circular initial data in the constant rotational velocity approach, i.e. they are consistent with Einstein equations and in hydrodynamical equilibrium. We study the NS rotation effect on the energetics, the gravitational waves (GWs) and on the possible electromagnetic (EM) emission associated to dynamical mass ejecta. For dimensionless spin magnitudes of $\chi \sim 0.1$ we find that spin-orbit interactions and also spin-induced–quadrupole deformations affect the late-inspiral–merger dynamics. The latter is, however, dominated by finite-size effects. Spin (tidal) effects contribute to GW phase differences up to ~ 5 (20) radians accumulated during the last eight orbits to merger. Similarly, after merger the collapse time of the remnant and the GW spectrogram are affected by the NSs rotation. Spin effects in dynamical ejecta are clearly observed in unequal mass systems in which mass ejection originates from the tidal tail of the companion. Consequently kilonovae and other EM counterparts are affected by spins. We find that spin aligned to the orbital angular momentum leads to brighter EM counterparts than antialigned spin with luminosities up to a factor of two higher.

PACS numbers: 04.25.D-, 04.30.Db, 95.30.Lz, 97.60.Jd

I. INTRODUCTION

With the detection of the first gravitational wave (GW) signals GW150914 [2] and GW151226 [3] the era of GW astronomy has begun. Beside black hole binaries, binary neutron stars (BNS) are one of the expected sources for future detections with the advanced GW interferometers [4]. The theoretical modeling of the GW signal is crucial to support future GW astronomy observation of BNS. BNS mergers are also expected to be bright in the electromagnetic (EM) spectrum. Possible EM counterparts of the GW signal are short gamma-ray bursts [5–7], kilonovae [8–11] (also referred to as macronovae) and radio flares [12]. Detailed models of EM counterparts will help the development of multimessenger astronomy.

Modeling BNS mergers requires to cover the entire parameter space of BNSs, including the stars' rotational (spin) effects. Although observations suggest that most neutron stars (NSs) in binary systems have comparable individual masses $\sim 1.35 M_\odot$ and relatively small spins [13, 14], this conclusion might be biased by the small number of observed BNS. The BNS parameter space could be much richer, in particular population synthesis models predict a wider range of masses and mass ratios [15, 16]. Recent observations of compact binary systems with mass ratios of $q \approx 1.3$ suggest that BNSs with a significant mass asymmetry can exist [17, 18]. As far as spins are concerned, pulsar data indicate that NS can have a significant rotation even in binary systems. Some of these NS in binaries approach the rotational frequency of isolated milli-second pulsars.

For example, the NS in the binary system PSR J1807−2500B has a rotation frequency of 239Hz [14, 19], and one of the double pulsar components (PSR J0737−3039A) has rotational a frequency of 44Hz [20]. There is also evidence that dynamical capture and exchange interactions involving NSs are a frequent occurrence in globular clusters [21]; during this process exotic objects, such as double millisecond pulsars might form [22].

The only possibility to study the dynamics and waveforms in the time period shortly before and after the merger of BNS systems is to perform numerical relativity (NR) simulations that include general relativistic hydrodynamics (GRHD). Despite the large progress of the field during the last 10 years, spin effects in BNS mergers have been investigated in few works. A main reason was the lack of consistent and realistic initial data for the simulations, a crucial prerequisite for NR evolutions. General-relativistic quasi-equilibrium configurations of rotating NSs of circular binary system can be now computed within the constant rotational velocity (CRV) approach [23, 24]. These data are neither corotational nor irrotational, and permit, for the first time, the NR-GW modeling of realistic BNS sources with spins. (See Sec. I of [25] for a discussion). Alternative NR evolutions of spinning BNS were presented in [26–29], but employed constraint violating initial data. Spinning BNS were also considered with a smooth particle hydrodynamics code under the assumption of conformal flatness, e.g. [30].

Evolutions of CRV initial data have been considered in [16, 25, 31]. We have presented the first evolutions covering the last 3 orbits and postmerger for a BNS systems described by polytropic equations of state [25]. That work proposed an analysis of the conservative dynamics in terms of gauge-invariant curves of the binding energy vs. angular momentum and a very preliminary analysis of the spin effects on the waveform. In [16] we have made significant improvements in the way we construct CRV initial data, which allows us to investigate BNS mergers in an extended parameter space, and presented preliminary evolutions of generic mergers (i.e. with precession). Ref. [31] presented an independent implementation of CRV initial data and preliminary evolutions, but did not cover the final merger and postmerger phases.

Several important questions remain open. A detailed understanding of the role of spin interactions will be fundamental for building analytical models of the inspiral–merger phase. Thus, it is important to further explore the BNS dynamics with long simulations and spanning a larger parameter space than previously considered. The influence of the NS spins on the GW phase evolution during the last orbits and up to merger is not fully understood but is very relevant for GW data analysis [32, 33]. Understanding the spin influence on the merger remnant might be relevant for both GW and EM observations. Also, the role of the NSs rotation on the dynamical ejecta and on the EM counterparts has not been explored.

In this article, we investigate rotational (spin) effects in multi-orbit BNS merger simulations with different mass-ratio and propose the first answers to the questions above. Our simulations cover ~ 12 orbits to merger and postmerger for mass ratios $q = 1, 1.25, 1.5$, two different equations of state (EOSs), and spin aligned or antialigned to the orbital angular momentum. These simulations are the first of their kind, and will support the development of analytical models of the GWs and of the EM emission from merger events. This paper extends the results of Ref. [1] (hereafter Paper I) that was limited to irrotational configurations and focused on the effect of the mass ratio. Our goal is to cover a significant part of the BNS parameter space.

The article is structured as follows: In Sec. II, we describe briefly the numerical methods and some analysis tools. In Sec. III we present the configurations employed in this work. Section IV summarizes the dynamics of the merger process, where the spin evolution of the individual stars and the energetics during the inspiral and postmerger are discussed. In Sec. V-VII dynamical ejecta, the GW signal, and possible electromagnetic (EM) counterparts are studied. We conclude in Sec. VIII.

Throughout this work we use geometric units, setting $c = G = M_\odot = 1$, though we will sometimes include $M_\odot$ explicitly or quote values in cgs units for better understanding and astrophysical interpretation. Spatial indices are denoted by Latin letters running from 1 to 3 and Greek letters are used for spacetime indices running from 0 to 3.

II. SIMULATION METHODS

A. Initial configurations

Our initial configurations are constructed with the pseudospectral SGRID code [16, 34–36]. We use the conformal thin sandwich equations [37–39] together with the CRV approach [23, 24] to solve the constraint equations. We construct quasi-equilibrium configuration in quasi-circular orbits, assuming a helical Killing vector. We follow exactly the same setup as in Paper I to which we refer for more details.

In order to construct BNS with different spins the approach of [16, 36] is adopted. The CRV method does not allow to prescribe the spin (or the dimensionless spin) directly; only the rotational part of the four-velocity can be specified as free data. We use Eq. (C3) of Ref. [16] to obtain an estimate for the four-velocity corresponding to a given dimensionless spin of $\chi = 0.1$. Once the rotational velocity is fixed, we compute a single NS with the same baryonic mass as the one in the binary and measure its ADM angular momentum. This gives the dimensionless spin of one component of the binary. The procedure is repeated for the other component.

For binary configurations in quasi-equilibrium, the described procedure gives consistent results between the ADM angular momentum of the spinning and irrotational BNS. In particular the difference between the $J_{\rm ADM}$ of the spinning and irrotational BNS is consistent with the sum of the spin estimates, $\Delta J_{\rm ADM} \sim (S^A + S^B)$, up to 10^{-2}; fractional errors are always $\lesssim 0.3\%$. Those small differences might also be caused by small differences in the initial orbital frequency.

The properties of the initial BNS configuration are summarized in Tab. I, and discussed in more detail in Sec. III.

B. Evolutions

Dynamical simulations are performed with the BAM code [40–42], employing the Z4c scheme [43, 44] and the 1+log and gamma-driver conditions for the gauge system [45–47]. The GRHD equations are solved in conservative form by defining Eulerian conservative variables from the rest-mass density ρ, pressure p, internal energy ϵ, and 3-velocity v^i with a high-resolution-shock-capturing method [40] based on primitive reconstruction and the Local-Lax-Friedrichs central scheme for the numerical fluxes. The GRHD system is closed by an EOS. We work with two EOSs modeled as piecewise polytropic fits [1, 48] and include thermal effects with an additive pressure contribution $p_{\rm th} = (\Gamma_{\rm th} - 1)\rho\epsilon$ [49, 50] setting $\Gamma_{\rm th} = 1.75$. The Berger-Oliger algorithm is employed for the time stepping [51] and we make use of an additional refluxing algorithm to enforce mass conservation across mesh refinement boundaries [52, 53] as in previous works [1, 42, 54]. Restriction and prolongation be-

TABLE I. BNS configurations. The first column defines the configuration name. Next 9 columns describe the physical properties of the single stars: the EOS, the gravitational masses of the individual stars $M^{A,B}$, the baryonic masses of the individual stars $M_b^{A,B}$, the stars' spins $S^{A,B}$, and dimensionless spins $\chi^{A,B}$. The last 5 columns define the tidal coupling constant κ_2^T, the mass-weighted spin χ_{mw}, the initial GW frequency $M\omega_{22}^0$, the ADM-Mass $M_{\rm ADM}$, and the ADM-angular momentum $J_{\rm ADM}$.

	Name	EOS	M^A	M^B	M_b^A	M_b^B	S^A	S^B	χ^A	χ^B	κ_2^T	$\chi_{\rm mw}$	$M\omega_{22}^0$	M_{ADM}	J_{ADM}
$q=1.00$	ALF2-137137$^{(00)}$	ALF2	1.375008	1.375008	1.518152	1.518152	0.0000	0.0000	0.000	0.000	125	0.000	0.0360	2.728344	8.1200
	ALF2-137137$^{(\uparrow\uparrow)}$	ALF2	1.375516	1.375516	1.518152	1.518152	0.1936	0.1936	0.102	0.102	125	0.102	0.0360	2.729319	8.4811
	ALF2-137137$^{(\uparrow\downarrow)}$	ALF2	1.375516	1.375516	1.518152	1.518152	0.1936	-0.1936	0.102	-0.102	125	0.000	0.0360	2.729333	8.1240
	ALF2-137137$^{(\uparrow 0)}$	ALF2	1.375516	1.375008	1.518152	1.518152	0.0000	0.1936	0.102	0.000	125	0.051	0.0360	2.728816	8.2997
$q=1.00$	H4-137137$^{(00)}$	H4	1.375006	1.375006	1.498528	1.498528	0.0000	0.0000	0.000	0.000	188	0.000	0.0348	2.728211	8.0934
	H4-137137$^{(\uparrow\uparrow)}$	H4	1.375440	1.375440	1.498528	1.498528	0.1892	0.1892	0.100	0.100	188	0.100	0.0348	2.729056	8.4508
	H4-137137$^{(\uparrow\downarrow)}$	H4	1.375440	1.375440	1.498528	1.498528	0.1892	-0.1892	0.100	-0.100	188	0.000	0.0349	2.729067	8.0983
	H4-137137$^{(\uparrow 0)}$	H4	1.375440	1.375006	1.498528	1.498528	0.1892	0.000	0.100	0.000	188	0.050	0.0348	2.728643	8.2711
$q=1.25$	ALF2-122153$^{(00)}$	ALF2	1.527790	1.222231	1.707041	1.334040	0.0000	0.0000	0.000	0.000	127	0.000	0.0357	2.728212	7.9556
	ALF2-122153$^{(\uparrow\uparrow)}$	ALF2	1.528484	1.222602	1.707041	1.334040	0.2430	0.1521	0.104	0.102	127	0.103	0.0357	2.729255	8.3300
	ALF2-122153$^{(\uparrow\downarrow)}$	ALF2	1.528484	1.222602	1.707041	1.334040	0.2430	-0.1521	0.104	-0.102	127	0.013	0.0358	2.729256	8.0479
	ALF2-122153$^{(\uparrow 0)}$	ALF2	1.528484	1.222231	1.707041	1.334040	0.2430	0.0000	0.104	0.000	127	0.058	0.0357	2.728907	8.1895
$q=1.25$	H4-122153$^{(00)}$	H4	1.527789	1.222228	1.683352	1.318080	0.0000	0.0000	0.000	0.000	193	0.000	0.0349	2.728675	8.0248
	H4-122153$^{(\uparrow\uparrow)}$	H4	1.528365	1.222546	1.683352	1.318080	0.2329	0.1499	0.100	0.100	193	0.100	0.0349	2.729567	8.3899
	H4-122153$^{(\uparrow\downarrow)}$	H4	1.528365	1.222546	1.683352	1.318080	0.2329	-0.1499	0.100	-0.100	193	0.011	0.0349	2.729585	8.1135
	H4-122153$^{(\uparrow 0)}$	H4	1.528365	1.222228	1.683352	1.318080	0.2329	0.0000	0.100	0.00	193	0.056	0.0349	2.729250	8.2491
$q=1.50$	ALF2-110165$^{(00)}$	ALF2	1.650015	1.100016	1.862057	1.189870	0.0000	0.0000	0.000	0.000	133	0.000	0.0356	2.728542	7.6852
	ALF2-110165$^{(\uparrow\uparrow)}$	ALF2	1.650924	1.100296	1.862057	1.189870	0.2919	0.1223	0.107	0.101	133	0.105	0.0355	2.729669	8.0732
	ALF2-110165$^{(\uparrow\downarrow)}$	ALF2	1.650924	1.100296	1.862057	1.189870	0.2919	-0.1223	0.107	-0.101	133	0.024	0.0355	2.729677	7.8475
	ALF2-110165$^{(\uparrow 0)}$	ALF2	1.650924	1.100016	1.862057	1.189870	0.2919	0.0000	0.107	0.000	133	0.064	0.0355	2.729404	7.9599
$q=1.50$	H4-110165$^{(00)}$	H4	1.650017	1.100006	1.834799	1.176579	0.0000	0.0000	0.000	0.000	209	0.000	0.0350	2.729385	7.81991
	H4-110165$^{(\uparrow\uparrow)}$	H4	1.650752	1.100242	1.834799	1.176579	0.2745	0.1204	0.101	0.099	209	0.100	0.0350	2.730283	8.18713
	H4-110165$^{(\uparrow\downarrow)}$	H4	1.650752	1.100242	1.834799	1.176579	0.2745	0.1204	0.101	-0.099	209	0.021	0.0350	2.730267	7.96085
	H4-110165$^{(\uparrow 0)}$	H4	1.650752	1.100006	1.834799	1.176579	0.2745	0.0000	0.101	0.000	209	0.061	0.0350	2.730050	8.07357

TABLE II. Grid configuration: name, EOS, finest grid spacing h_{L-1}, radial resolution inside the shells h_r, number of points n (n^{mv}) in the fixed (moving) levels, radial point number n_r and azimuthal number of points n_θ in the shells, inradius up to which GRHD equations are solved r_1, and the outer boundary r_b.

Name	EOS	h_{L-1}	h_r	n	n^{mv}	n_r	n_θ	r_1	r_b
R1	ALF2	0.250	8.00	128	64	128	64	572	1564
R2	ALF2	0.167	5.33	192	96	192	96	552	1555
R1	H4	0.250	8.00	128	72	128	64	572	1564
R2	H4	0.167	5.33	192	108	192	96	552	1555

tween the refinement levels is performed with an average scheme and 2nd order essentially non-oscillatory scheme, respectively.

We employ the same grid setup as the "shell" setup in Paper I, i.e. the numerical domain is made of a hierarchy of cell-centered nested Cartesian grids, where the outermost level is substituted by a multipatch (cubed-sphere) grid [44, 55–57]. In total we have used 4 different grid setups summarized in Tab. II.

C. Simulation analysis

Most of our analysis tools were summarized in Sec. III of Paper I. They include the computation of the ejecta quantities, the disk masses, the entropy indicator, the amount of mass transfer during the inspiral, and the way we extract GWs. Here, we extend the analysis tools by including a quasi-local measure of the spin of the NSs. Following a similar approach as in Refs. [31], we evaluate the surface integral

$$S^i \approx \frac{1}{8\pi}\int_{r_s} \mathrm{d}^2x\sqrt{\gamma}\left(\gamma^{kj}K_{lk}-\delta^j_l K\right)n_j\varphi^{li}, \qquad (1)$$

on coordinate spheres with radius r_S around the NSs. $\varphi^{li}=\epsilon^{lik}x_k$ defines the approximate rotational Killing vectors in Cartesian coordinates $(\varphi^{l1},\varphi^{l2},\varphi^{l3})$, K_{ij} denotes the extrinsic curvature, γ^{ij} the inverse 3-metric, and $n_i=(x_i-x_i^{\rm NS})/r$ the normal vector with respect to the center of the NS. The center is given by the min-

imum of the lapse inside the NS[1]. Differently from [31] we do not determine the center of the coordinate sphere by the maximum density and we do not use comoving coordinates in our simulations.

Let us discuss the interpretation of Equation (1). For equilibrium rotating NS spacetimes, Eq. (1) in the limit $r_S \to \infty$ reproduces the ADM angular momentum of the (isolated) NS, see Appendix A. In dynamical BNS evolutions, Eq. (1) allows us to measure the spin evolution and spin direction. We stress that, in the BNS case, the spin measure has some caveats: (i) no unambiguous spin definition of a single object inside a binary system exists in general relativity; (ii) Eq. (1) is evaluated in the strong-field region although it is only well defined at spatial infinity; (iii) the r_S spheres are gauge dependent.

III. BNS CONFIGURATIONS

We consider BNS configurations with fixed total mass of $M = M^A + M^B = 2.75 M_\odot$, and vary EOS, mass-ratio, and the spins. The spins are always aligned or antialigned to the orbital angular momentum. The EOSs are ALF2 and H4; both support masses of isolated NSs above $2M_\odot$ and are compatible with current astrophysical constraints. We vary the mass ratio,

$$q := \frac{M^A}{M^B} \geq 1 \ , \tag{2}$$

spanning the values $q = (1.0, 1.25, 1.5)$. For every EOS and q, we consider four different spin configurations:

(00) none of the stars is spinning;

(↑↑) both spins are aligned with the orbital momentum;

(↑↓) the spin of star A is aligned, the other star spin is anti-aligned;

(↑ 0) the spin of star A is aligned to the orbital angular momentum and the other NS is considered to be irrotational,

where the dimensionless spin magnitude

$$\chi := \frac{S}{M^2} \tag{3}$$

of each star is either $\chi = 0$ or $\chi \sim 0.1$. The properties of the considered BNSs are summarized in Tab. I.

A BNS configuration is determined by its EOS, individual masses (or mass ratio), and the two spins. Focusing on the GWs, we parametrize this configuration space as follows. Spin effects are described by the mass-weighted spin combination,

$$\chi_{\rm mw} := \frac{M^A \chi^A + M^B \chi^B}{(M^A + M^B)} \ , \tag{4}$$

which is used for phenomenological waveforms models and during GW searches, e.g. [59, 60]. The mass-weighted spin is related to the effective spin χ_ϕ, which captures the leading order spin effects of the phase evolution via

$$\chi_\phi = \chi_{\rm mw} - \frac{38\nu}{113}(\chi^A + \chi^B) \ , \tag{5}$$

with the symmetric mass ratio $\nu = M^A M^B/(M^A + M^B)^2$. For the setups presented here $\chi_{\rm mw} \approx \chi_{\rm eff}$, which is the reason why we restrict us to the more commonly used $\chi_{\rm mw}$.

Most of the NS structure and EOS information is encoded in the tidal polarizability coefficient [61, 62]

$$\kappa_2^T := 2\left(\frac{q^4}{(1+q)^5}\frac{k_2^A}{C_A^5} + \frac{q}{(1+q)^5}\frac{k_2^B}{C_B^5}\right) \tag{6}$$

that describes at leading order the NSs' tidal interactions. κ_2^T depends on the EOS via the quadrupolar dimensionless Love number k_2 of isolated spherical star configurations, e.g. [63], and the compactness C of the irrotational stars (defined as the ratio of the gravitational mass in isolation with the star's proper radius). As a further parameter we choose the mass ratio, since the dynamics of nonspinning black hole binary is entirely described by q.

The 3D parametrization $(q, \chi_{\rm mw}, \kappa_2^T)$ is a (possible) minimal choice for the description of BNS GWs. The binary total mass M, in particular, scales trivially in absence of tides and its dependency in the tidal waveform is hidden in the κ_2^T, to leading order. It should be noted, however, that $(q, \chi_{\rm mw}, \kappa_2^T)$ are not independent variables and some degeneracies exists [κ_2^T and $\chi_{\rm mw}$ depend on q for instance]. Furthermore, we note that the intrinsic NS rotation can also influence tidal effects during the evolution. In this work, we use for consistency $(q, \chi_{\rm mw}, \kappa_2^T)$ to study the parametric dependency of other quantities than GWs, like ejecta and EM luminosity.

The $(q, \chi_{\rm mw}, \kappa_2^T)$ parameter space coverage of our work is shown in Fig. 1. In total we are considering 24 BNSs. The irrotational configurations were already presented in Paper I, but 36 new simulations were performed for the scope of this paper. Every configuration is simulated with two different resolutions R1 and R2, see Tab. II. This allows us to place error bars on our results, which will be conservatively estimated as the difference between the resolutions, see [64, 65] for a detailed analysis.

[1] While this paper has been written also [58] implemented the exactly same method as proposed here to measure the spin of the single NSs during BNS inspirals. Both implementations have been compared and give similar results.

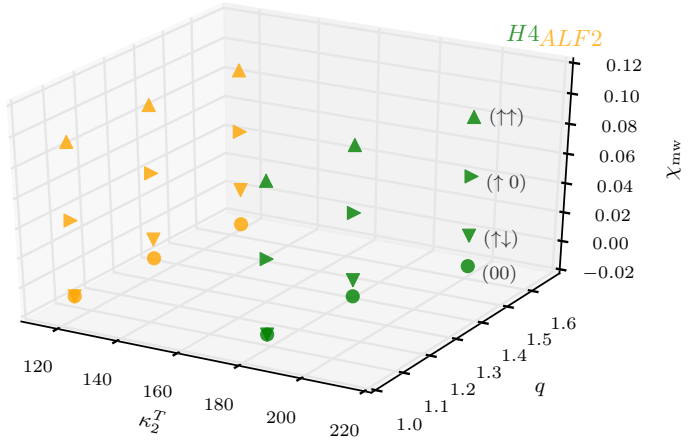

FIG. 1. The $(q, \chi_{\rm mw}, \kappa_2^T)$ parameter space coverage. Different colors refer to the EOS ALF2 (orange) and H4 (green). Different markers correspond to different spin configurations: circles (00), triangles pointing down (↑↓), triangles pointing right (↑ 0), and triangles pointing up (↑↑).

IV. DYNAMICS

A. Qualitative discussion

Our simulations span $N_{\rm orb} \sim 10 - 12$ orbits (20-24 GW cycles) to merger, the number of orbits increases (decreases) for spin aligned (antialigned) to the orbital angular momentum. In this regime, spin effects typically contribute up to $\Delta N_{Spin} \sim \pm 1$ orbits. The spin effect is comparable to the effect of the EOS variation and of the mass ratio, $\Delta N_{\rm EOS} \sim \Delta N_q \sim \Delta N_{Spin}$. BNS with stiffer EOS and/or larger q take fewer orbits to merge for a fixed initial GW frequency[2].

Figure 2 shows the rest-mass density profile inside the orbital plane for the configurations employing the H4 EOS with resolution R2. The snapshots are taken at the moment of merger, i.e., at the time where the amplitude of the GW has its maximum.

Although the initial orbital frequency is almost identical for all systems with the same mass-ratio and EOS, cf. Tab. I, the "orbital phase" at the moment of merger differs due to the spin of the individual stars. In general, if a NS has spin aligned to the orbital angular momentum, the binary dynamics is less bound leading to a slower phase evolution with respect to the irrotational case. Contrary, if a NS has anti-aligned spin the binary is more bound leading to a faster phase evolution and an earlier moment of merger, i.e. at lower frequencies (see Sec. VI). This *spin-orbit* (SO) effect has a solid analytical basis [66], and was already reported in both BBH simulations [67] ("orbital hang-up" effect) and in BNS setups [16, 25–27].

[2] Recall that for our configurations the H4 EOS is stiffer than the ALF2 EOS.

In the BNS configurations with (↑↓) and equal masses ($q = 1$) the SO effect is zero at leading order, cf. Eq. (12) and discussion below. Notably in these cases, the effects of the *spin-spin* interactions (SS) are observed in our simulations. Comparing the irrotational BNS (00) with the (↑↓) configuration, the latter has a faster phase evolution, i.e. merges at lower frequencies.

After merger, the simulations are continued for about $\sim$ 30ms. All the BNS considered in this work form a hypermassive neutron star (HMNS). The presence of spin influences the angular momentum of the remnant HMNS. Configurations with (↑↑), for example, have additional angular momentum support and the HMNS has a longer lifetime. Spin effects influence the HMNS's rotation law and its dynamical evolution [see Sec. VI B for a detailed discussion]. Overall, spin effects are observed in the remnant and ejecta, but better resolved during the early part of the simulations.

B. Spin Evolution

The evolution of the quasi-local spin computed by Eq. (1), is shown in Fig. 3 for the representative case H4-137137$^{(\uparrow\downarrow)}$. We find that, within our uncertainties, the spins magnitudes remain roughly constant up to the actual collision of the two stars. When the two stars finally merge, there is a single surface integral, and Eq. (1) estimates the orbital angular momentum of the merger remnant. Our results are consistent with what was observed in [31], although the latter do not extend to merger. They are also consistent with BBH simulations in which spins remain roughly constant up to the formation of a common horizon [68–70]. However, comparing with [31] our results have larger uncertainties, whose origin we discuss in the following.

Fig. 3 shows that, during the evolution, the spin magnitude of the NS with spin aligned to the orbital angular momentum seems to be larger by $\sim$ 20% compared to the other. This happens despite the fact that the rotational velocities (and initial spin values) are initially of the same magnitude. A similar effect was shown in [31], but it is more pronounced in our setup.

We argue this is caused by the fact that we are using coordinate spheres in a non comoving coordinate system. As a result, our setup does not capture accurately the (approximate) rotational symmetry around each star, the latter being numerically entangled with the orbital motion. The spin magnitudes are, consequently, overestimated. For the same reason we observe a drift of the spin magnitude that increases the closer the merger is. We believe this effect is partially related to numerical accuracies. Note finally that for irrotational BNSs we measure a residual spin $S \sim 10^{-2}$. The value is consistent with the accuracy level of the initial data, see also our results on isolated stars in App. A.

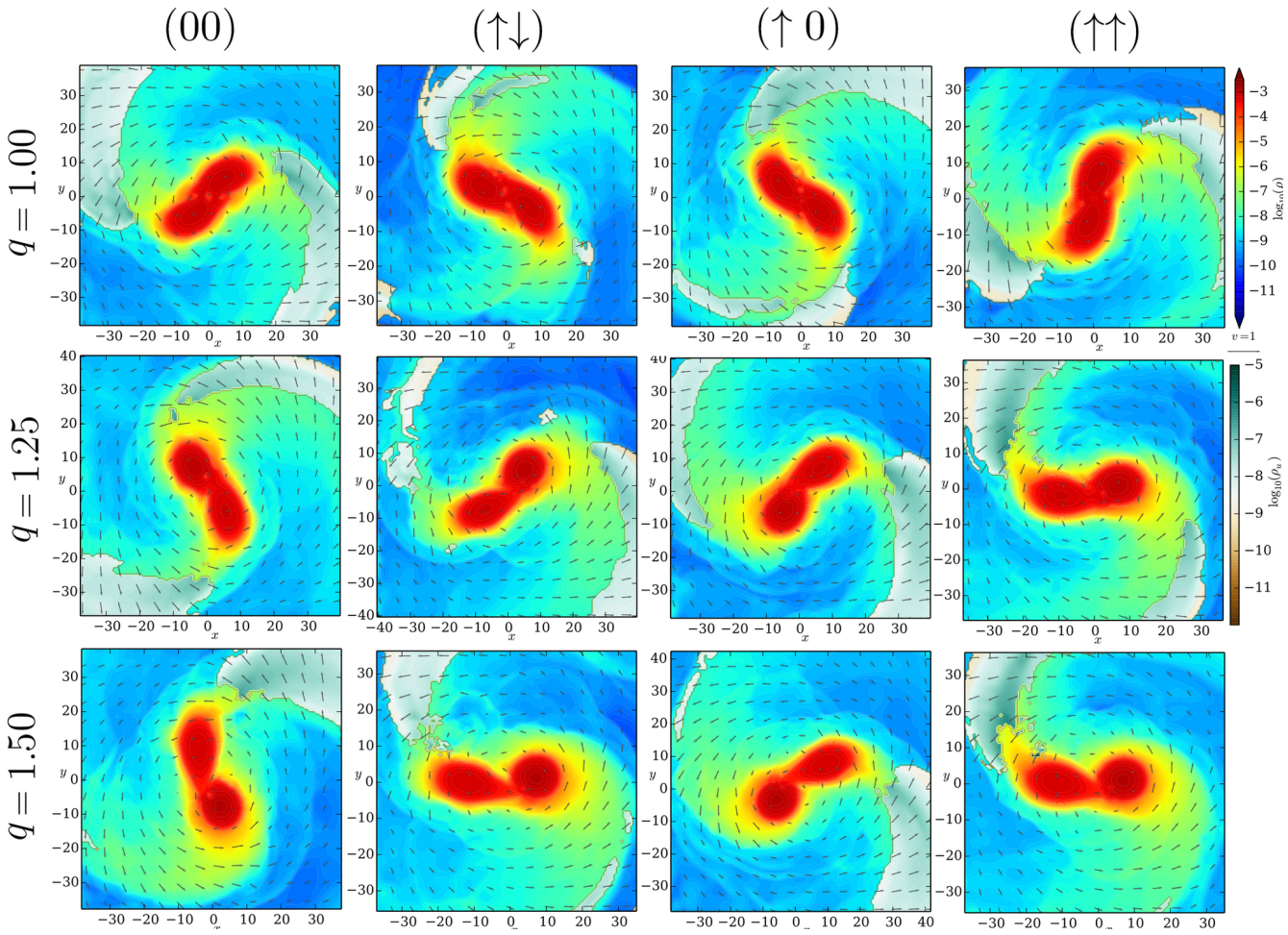

FIG. 2. Rest-mass density profile inside the orbital plane for simulations employing the H4 EOS and using the R2 grid setup. The snapshots represent the moments of merger. The panels refer to (from top to bottom) mass ratios $q = 1.00, q = 1.25, q = 1.50$ and (from left to right) spin configurations $(00), (\uparrow\downarrow), (\uparrow 0), (\uparrow\uparrow)$. The rest-mass density ρ is shown on a logarithmic scale from blue to red. The rest-mass density of unbound material is colored from brown to green. Most material gets ejected from the tidal tails of the NS inside the orbital plane.

C. Energetics

We now discuss the BNS dynamics at a quantitative level by considering the gauge invariant curves of the binding energy vs. orbital angular momentum [72] as well as the binding energy and angular momentum dependency on the orbital frequency.

The specific binding energy is given by

$$E_b = \frac{1}{\nu}\left[\frac{M_{\rm ADM}(t=0) - \mathcal{E}_{\rm rad}}{M} - 1\right] , \qquad (7)$$

where $\mathcal{E}_{\rm rad}$ is the energy emitted via GWs, as computed from the simulations (cf. Sec. V of Paper I). The specific and dimensionless orbital angular momentum is

$$\ell = \frac{L(t=0) - \mathcal{J}_{\rm rad}}{\nu M^2} , \qquad (8)$$

where $\mathcal{J}_{\rm rad}$ denotes the angular momentum emitted by GWs. L is the orbital angular momentum, a quantity that is not of direct access in our simulations. Thus, we approximate $L(t=0)$ by [16, 25]

$$L(t=0) = J_{\rm ADM}(t=0) - S^A - S^B, \qquad (9)$$

where $J_{\rm ADM}(t=0)$ is the ADM-angular momentum and $S^{A,B}$ the spins of the NSs measured in the initial data. We further assume that spins are approximately constant during the evolution, cf. Sec. IV B and [31].

In addition to the $E_b(\ell)$ curves we consider the binding energy and angular momentum as functions of the dimensionless parameter $x = (M\Omega)^{2/3}$, where Ω is the orbital frequency. The latter can be unambiguously calculated from the simulation as [62]

$$M\Omega = \frac{\partial E_b}{\partial \ell} . \qquad (10)$$

This quantity can be also used to characterize the post-merger dynamics as we do in Sec. IV C 2.

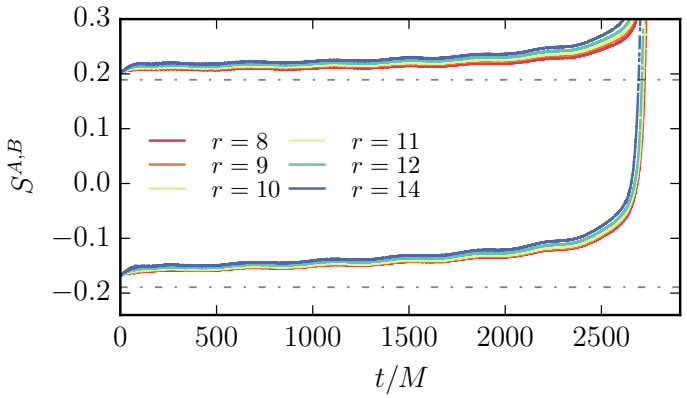

FIG. 3. Quasi-local measurement of the individual spin of the two NSs for H4-137137$^{(\uparrow\downarrow)}$. The gray dashed dotted lines in the diagram represent the value computed from the initial data solver and given in Tab. I. Different colors refer to different radii of the coordinate spheres. The increasing quasi-local spin is most likely caused by the choice of the center of the integration surface and by using a coordinate sphere not taking tidal deformations into account.

1. *Energetics: late inspiral–merger*

The $E_b(\ell)$ curves probe in a direct way the conservative dynamics of the binary [72]. In [25] we have proposed a simple way of analyzing energetics during the inspiral–merger that relies on extracting the individual contributions of the binary interactions, i.e. spin-orbit (SO), spin-spin (SS) and tidal (T). Our new simulations allow us to improve that analysis by extracting more accurately the SO and SS interaction contributions.

Motivated by the post-Newtonian (PN) formalism and building on [16, 25] we make the additive ansatz for the binding energy [we omit hereafter the subscript "b"]

$$E \approx E_0 + E_T + E_{SO} + E_{S^2} + E_{S\leftrightarrow S}, \tag{11}$$

where E_0 is a orbital (point-particle) term, E_T the tidal term, E_{SO} the SO term, E_{S^2} a SS term due self-coupling of the spin of the single star, i.e. a change of the quadrupole moment due to the intrinsic rotation, and $E_{S\leftrightarrow S}$ an SS interaction term due to the coupling of the stars' spins. Each of the above contributions corresponds to a term in the PN Hamiltonian. At leading order (LO) we have at 1.5PN

$$H_{SO} \approx \frac{2\nu L}{r^3} S_{\rm eff} \tag{12}$$

with the effective spin

$$S_{\rm eff} = \left(1 + \frac{3}{4}\frac{M^B}{M^A}\right)\bar{S}^A + \left(1 + \frac{3}{4}\frac{M^A}{M^B}\right)\bar{S}^B \tag{13}$$

and at 2PN

$$H_{S^2} \approx -\frac{\nu}{2r^3}\left(\frac{C_{Q_A} M^B}{M^A}\bar{S}_A^2 + \frac{C_{Q_B} M^A}{M^B}\bar{S}_B^2\right), \tag{14}$$

and

$$H_{S\leftrightarrow S} \approx -\frac{\nu}{r^3}\bar{S}^A\bar{S}^B, \tag{15}$$

with C_Q describing the quadrupole deformation due to spin, e.g. [73] and Appendix B, and $\bar{S}^A = q\chi^A$, $\bar{S}^B = \chi^B/q$.

Focusing on the equal mass configurations and applying the ansatz above to the binding energy of each configuration, we write

$$E^{(00)} \approx E_0 + E_T, \tag{16}$$
$$E^{(\uparrow\downarrow)} \approx E_0 + E_T + E^{(\uparrow\downarrow)}_{S\leftrightarrow S} + E^{(\uparrow\downarrow)}_{S^2}, \tag{17}$$
$$E^{(\uparrow 0)} \approx E_0 + E_T + E^{(\uparrow 0)}_{SO} + E^{(\uparrow 0)}_{S^2}, \tag{18}$$
$$E^{(\uparrow\uparrow)} \approx E_0 + E_T + E^{(\uparrow\uparrow)}_{SO} + E^{(\uparrow\uparrow)}_{S\leftrightarrow S} + E^{(\uparrow\uparrow)}_{S^2}. \tag{19}$$

We have omitted the superscript for the individual simulations for the E_0 and E_T contribution since we assume that they are the same for all setups. Using the simulation data we extract each contributions as follows. First, we consider an equal mass, non-spinning BBH-simulation to provide $E^{(\rm BBH)} \approx E_0$ [3]. Then, we use the relations

$$E^{(\uparrow\uparrow)}_{SO} \approx 2E^{(\uparrow 0)}_{SO} \ , \quad E^{(\uparrow\uparrow)}_{S^2} \approx 2E^{(\uparrow 0)}_{S^2}, \tag{20}$$
$$E^{(\uparrow\uparrow)}_{S^2} \approx E^{(\uparrow\downarrow)}_{S^2} \ , \quad E^{(\uparrow\uparrow)}_{S\leftrightarrow S} \approx -E^{(\uparrow\downarrow)}_{S\leftrightarrow S} \ , \tag{21}$$

that come from the LO expressions of the PN Hamiltonian above Eqs. (12)-(14)-(15) and from the fact that the stars have the same mass ($M^A = M^B$) and spin magnitudes ($S^A = S^B$). This way, based on the five different cases, the individual contributions read

$$E_T \approx E^{(00)} - E^{\rm BBH} \tag{22}$$
$$E^{(\uparrow\uparrow)}_{SO} \approx -2E^{(00)} - E^{(\uparrow\downarrow)} + 4E^{(\uparrow 0)} - E^{(\uparrow\uparrow)}, \tag{23}$$
$$E^{(\uparrow\uparrow)}_{S^2} \approx E^{(\uparrow\downarrow)} - 2E^{(\uparrow 0)} + E^{(\uparrow\uparrow)}, \tag{24}$$
$$E^{(\uparrow\uparrow)}_{S\leftrightarrow S} \approx E^{(00)} - 2E^{(\uparrow 0)} + E^{(\uparrow\uparrow)}. \tag{25}$$

All contributions are shown in Fig. 4 for the ALF2 EOS (left) and the H4 EOS (right). For comparison we include as a shaded region the difference between resolutions R1 and R2 for the individual components. The plot clearly shows the repulsive (attractive) character of the SO (tidal) interaction and quantifies each term for a fixed value of the orbital angular momentum. The plot indicates that, although poorly resolved, SS interactions might play a role close to merger. The E_{S^2} terms, in particular, are rather large for $\ell \lesssim 3.6$ and contribute to the merger dynamics with an effect opposed to the one of the SO interaction (note the negative sign of E_{S^2} in the plots). Summing up all the spin effects, we find that spin contributions are of the same order as tidal effects.

[3] The BBH $E_b(\ell)$ curve is computed with the SpEC code [74] and corresponds to SXS:BBH:0066 of the public catalog, see also [75].

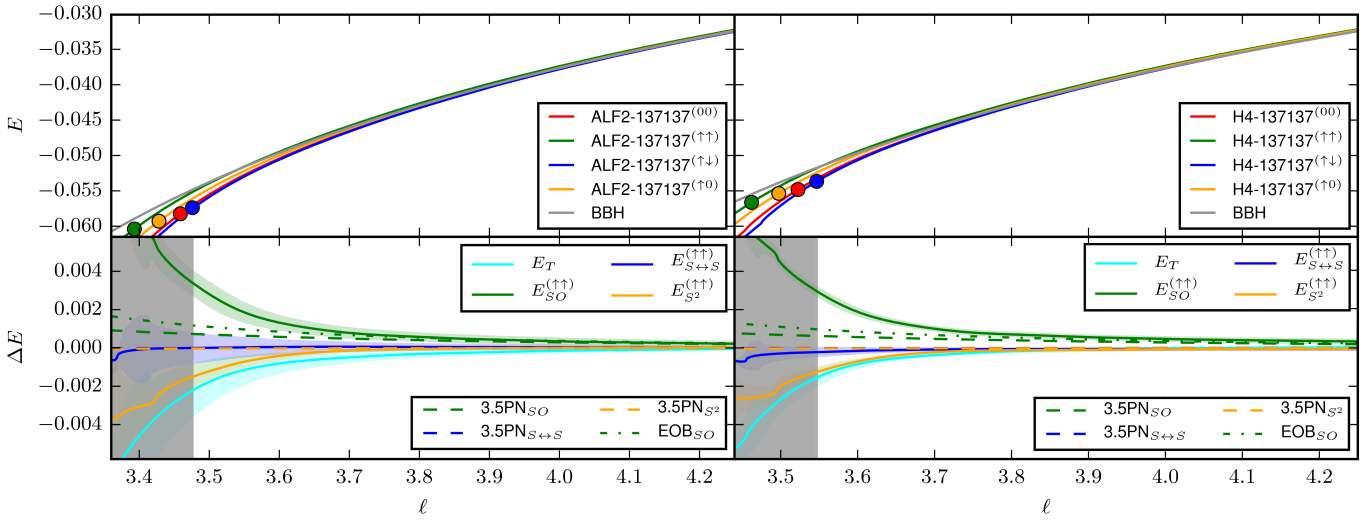

FIG. 4. Binding energy vs. specific angular momentum curves $E(\ell)$ for the equal mass configurations (upper panels). The circles mark the moment of merger for all configurations. We also include a non-spinning BBH configuration from the public SXS catalog, see text for more details. The bottom panels show the individual contributions to the binding energy, Eq. (11), we present the SO (green), S^2 (orange), $S \leftrightarrow S$ (blue) configurations obtained from the NR data as solid lines. For those contributions we also include 3.5PN (App. B) estimates as dashed lines. The tidal contributions are shown as cyan lines. We also include the SO contribution from the EOB model of [71]. We mark the difference between resolution R2 and R1 as a colored shaded region. The vertical gray areas correspond to the merger of the ALF2-137137$^{(\uparrow\downarrow)}$ (left) and the H4-137137$^{(\uparrow\downarrow)}$ configuration (right).

This demonstrates the importance of including spins in analytical models of BNS.

On top of our numerical results we plot 3.5PN estimates for SO, and SS interactions as dashed lines (see Appendix B for their explicit expressions) and the SO effective-one-body (EOB) estimate of [71] as dot-dashed lines. The SO term extracted from the NR data shows significant deviations from the EOB analytical results for $\ell \lesssim 3.6 - 3.7$, which correspond to GW frequencies of $M\omega_{22} \sim 0.073 - 0.083$ (compare with merger frequencies in Tab. IV). The EOB model is closer to the numerical data than the PN model, but underestimate (in absolute value) the magnitude of the SO term during the last 2-3 orbits. The PN description of SO couplings shows deviations already at $\ell \lesssim 3.8$, and it is very inaccurate for the description of the S^2 SS effects[4]. These findings suggest that, already at the level of the Hamiltonian, more analytical work is needed to describe the very last orbits of BNS.

Interestingly however, we note that the "cumulative" spin contribution SO+SS can be reasonably approximated by the considered EOB SO model solely (for the considered dynamical range). The reason for this might be that the attractive character of the SS interaction partially "compensates" the effect of the missing analytical information[5]. Let us consider the sum of all spin contributions, E_{Spin}, and assume it can be formally parametrized as the LO SO interaction (lowest order in spin)

$$E_{Spin} \approx 2\nu S_{\rm eff} \mathcal{E}_{Spin} \ . \tag{26}$$

Consequently, Eq. (11) simplifies to

$$E \approx E_0 + E_T + 2\nu S_{\rm eff} \mathcal{E}_{Spin} \ , \tag{27}$$

and, by subtracting the non-spinning binding energy curves from the curves for spinning configurations, we calculate $\mathcal{E}_{Spin}$. Figure 5 presents our results. For this analysis we also include unequal mass configurations for which it was not possible to extract the individual contributions to the binding energy as done above for the equal mass cases. Notice that for an unequal mass system also $(\uparrow\downarrow)$ configurations contain SO-interactions, see cyan line. In the top panel we compare simulations for different EOS. The quantity $\mathcal{E}_{Spin}$ is the same for all simulations independent of the EOS. The bottom panel of Fig. 5 shows the effect of the mass ratio on $\mathcal{E}_{Spin}$, where again up to the merger all estimates agree. The EOB SO curve for $\mathcal{E}_{Spin}$ are closer to the NR data in this cases than in the one presented in Fig. 4.

[4] Note, however, that the ansatz in (11) might be inaccurate at high-frequency, and that our analysis might break close to merger. Furthermore, higher resolved simulations are needed to reduce the uncertainties extracting SS contributions.

[5] Let us also point out that extracting E_{Spin} is effected by smaller numerical uncertainties since only two different BNS configurations have to be considered, instead of four setups for E_{SO}.

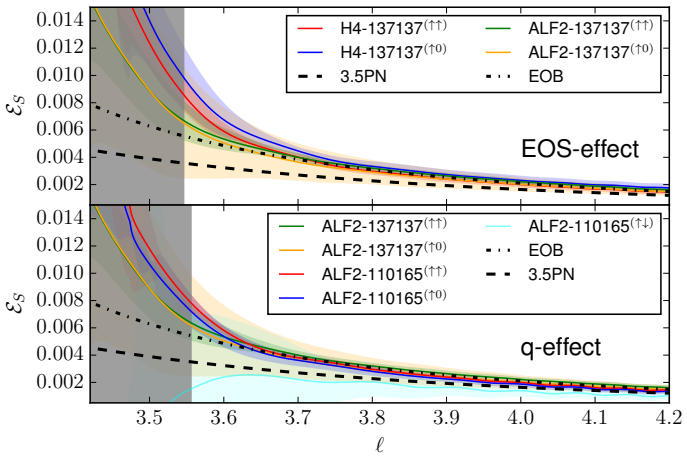

FIG. 5. Quantity $\mathcal{E}_{Spin}$ for different EOS and the same mass ratio ($q = 1.0$) in the top panel and for the same EOS (ALF2), but mass ratios $q = 1.0$ and $q = 1.5$ in the bottom panel. The colored shaded regions mark the difference between the results for resolution R2 and R1. Notice that for an unequal mass merger also the ($\uparrow\downarrow$) configuration contains SO-contributions and therefore could be included for $q = 1.5$ although the late time behavior is dominated by the SS-interactions. The vertical gray areas correspond to the moment of merger for H4-137137$^{(\uparrow 0)}$ (upper panel) and ALF2-110165$^{(\uparrow\downarrow)}$ (lower panel). We also include the 3.5PN SO contribution as a dashed line and EOB $\mathcal{E}_{Spin}$ as present in the EOB model of [71] as a dashed dotted line.

We finally discuss the curves $E_b(x)$ and $\ell(x)$, i.e., compare BNS energetics at fixed orbital frequency Ω. Figure 6 summarizes the equal mass results for ALF2 EOS (left) and the H4 EOS (right). The figure shows that once we consider systems with the same orbital frequency tidal contributions to the binding energy are larger than spin contributions. This becomes more visible in Fig. 7 for which we have extracted the individual components following Eq. (22)-(25).

Figure 7 also shows that the individual contributions to $E_b(x)$ and $E_b(\ell)$ have opposite signs. This can be understood by considering $\ell \propto \Omega r^2$ and $E \propto -r^{-1}$.

Let us first focus on tidal effects comparing a BBH and a BNS system. Because of the attractive nature of tidal effects $E_{b,\rm BBH} > E_{b,\rm BNS}$ (but $|E_{b,\rm BBH}| < |E_{b,\rm BNS}|$) for fixed angular momentum. Consequently $\Omega_{\rm BBH} < \Omega_{\rm BNS}$, which explains the inverse ordering of $E_b(x)$ and $E_b(\ell)$. Another approach is to consider the $\ell(x)$ curves for a fixed frequency for which $\ell_{\rm BNS} > \ell_{\rm BBH}$ and $r_{\rm BNS} > r_{\rm BBH}$. Therefore, the system is less bound, i.e. $E_{b,\rm BNS} > E_{b,\rm BBH}$, which is reflected in the $E(x)$ curves. In analogy it is possible to explain why E_{SO} and other spin dependent contributions have opposite signs if $E_b(x)$ and $E_b(\ell)$ are compared.

This also shows that while $E_b(\ell)$ curves can be directly used to understand the effect of individual components on the conservative dynamics, the interpretation of $E_b(x)$ is more subtle, but will be useful for the phase analysis of the system presented in Sec. VI.

2. *Energetics: postmerger*

Binding energy vs. specific angular momentum curves can be used also to study post-merger dynamics [62]. The frequency $M\Omega = \partial E_b/\partial \ell$, in particular, gives the rotation frequency of the HMNS merger remnant, and matches extremely well half the postmerger GW frequency. Spins effects are clearly visible at merger [25] but also in the postmerger Ω, especially in cases in which the merger remnant collapses to a black hole.

In Fig. 8 $E_b(\ell)$ and $M\Omega$ are presented for all configurations employing the H4 EOS. When the postmerger $E_b(\ell)$ are approximately linear, the rotational (and emission) frequency Ω remains steady for several milliseconds.

Comparable masses BNS remnant collapse to black hole within the simulated times (left panels) and Ω increases continuously up to the collapse. The continuous evolution of Ω (a "post-merger chirp" [1, 62]) is caused by the increasing compactness and rotational velocity of the remnant. Spins aligned to orbital angular momentum increase the angular momentum support of the remnant that, therefore, collapses later in time and at smaller values of ℓ. The remnant of configuration ($\uparrow\downarrow$) has a very similar dynamics to the one of (00).

The remnants of $q = 1.5$ BNS instead do not collapse during the simulated time. Interestingly, Ω shows a sharp jump right after merger and then remains approximately constant. The jump is only present in the $q = 1.5$ mass ratio setups. It originates from the secondary star whose core "falls" onto the primary star, after a partial tidal disruption. Consequently, the the rotational frequency of the merger remnant experience a rapid increase over a short time.

V. EJECTA

In Paper I we have pointed out that the amount of ejected material depends significantly on the mass-ratio where the ejecta mass increases for higher mass ratios with a linear behavior in q. In large-q BNSs the mass-ejection from the tidal tail of the companion (centrifugal effect) dominates the one originating from the cores' collision and the subsequent shock-wave. For the same reason, stiffer EOS favor larger mass ejection over softer EOS. The effect of the stars' rotation (dimensionless spins $\chi \sim 0.1$) on the dynamical ejecta are sub-dominant with respect to the mass-ratio and, to some extend, also to varying the EOS. We find that for configurations with large mass ratio ($q = 1.5$) the amount of ejecta is increasing from ($\uparrow\downarrow$) to ($\uparrow 0$), and to ($\uparrow\uparrow$) due to the progressively larger angular momentum in the tidal tail of the companion. We also identify a spin effects on the unbound material, as discussed below.

Figure 9 shows the most important ejecta quantities and their dependence on the spin and the mass ratio. We report the total ejecta mass $M_{\rm ej}$, the kinetic energy of the ejecta $T_{\rm ej}$, and the average velocities inside the or-

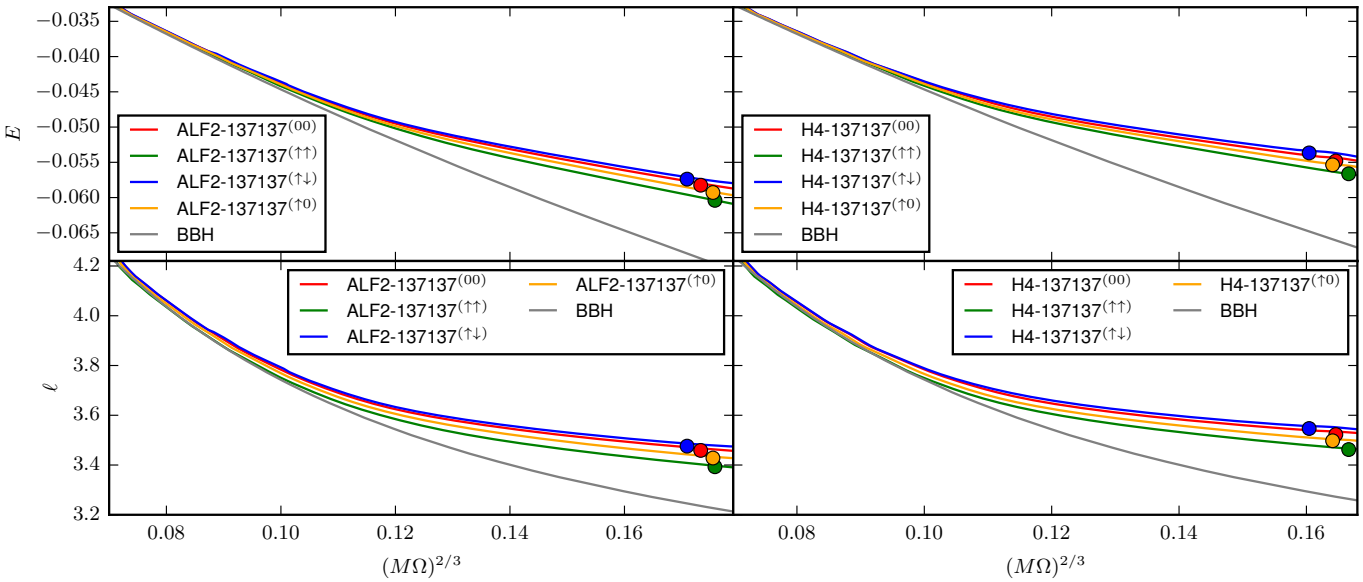

FIG. 6. Binding energy (top panels) and specific angular momentum (bottom panels) as a function of the PN parameter x. The circles mark the moment of merger for all configurations. We also include a non-spinning BBH configuration from the public SXS catalog as in Fig. 4. We have applied a Savitzky Golay filter on $E(x)$ and $\ell(x)$ to reduce numerical noise and eccentricity oscillations.

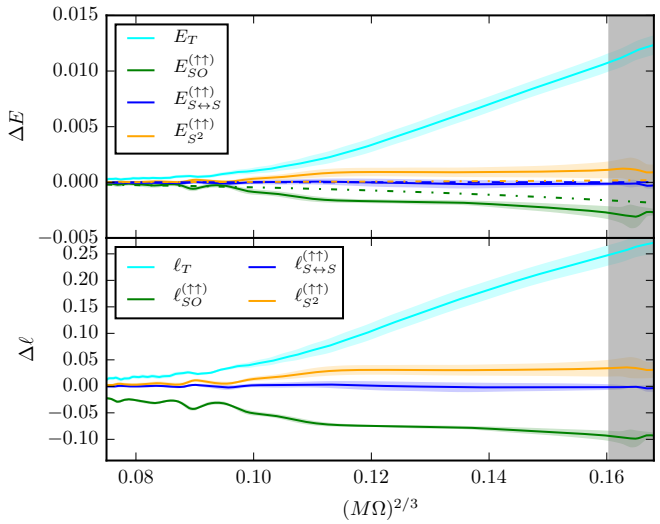

FIG. 7. Individual contributions to the binding energy (top panels) and specific angular momentum (bottom panels) as a function of the PN parameter $x = (M\Omega)^{2/3}$ for the equal mass systems employing the H4 EOS. The colored shaded regions mark the difference between resolution R2 and R1. The initial oscillations are caused mostly by remaining eccentricity effects not fully removed after applying the Savitzky Golay filter to $E(x)$ and $\ell(x)$. We also include 3.5PN estimates for the binding energy (App. B) as dashed dotted lines. The vertical gray line corresponds to the merger point of the H4-137137$^{(\uparrow\downarrow)}$.

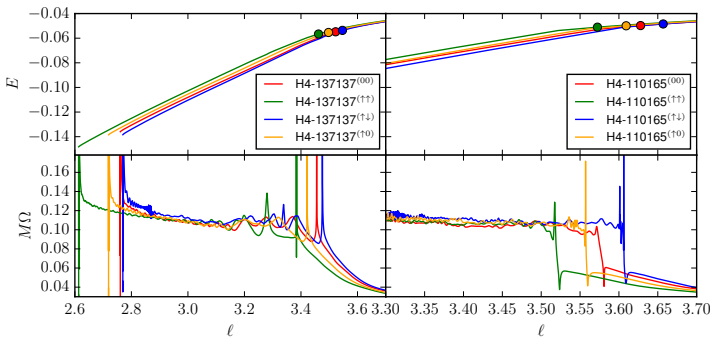

FIG. 8. Binding energy vs. specific angular momentum curves after the merger of the two neutron stars for the H4 setups with mass ratio $q = 1.0$ (left) and $q = 1.50$ (right). The merger is marked as a circle for all setups. The bottom panels present the frequency $M\Omega$ estimated from the binding energy curves.

bital plane $\langle|v_\rho|\rangle$ and perpendicular to the orbital plane $\langle|v_z|\rangle$ [see Paper I for more details]. The difference between resolution R2 and R1 is used as an error estimate and marked as an error bar. In the left panels results for $q = 1.00$ are shown and results for $q = 1.50$ are shown in the right panels. Different EOSs are colored differently: ALF2 (orange), H4 (green); and different markers represent the different spin configurations as in Fig. 1. More details about the ejecta are given in Tab. III.

For all configurations (independent of the spin) the ejecta mass is larger for larger mass ratios. A similar statement is true for the kinetic energy of the ejecta (second panel of Fig. 9). The EOS variation considered here does not show significant differences in the ejecta. Mass ejection in $q = 1$ BNS mostly originates from the shock wave that forms during the core collision, while in $q = 1.5$ BNS mostly originates form the tidal tail.

The influence of the NS spin is smaller than the ef-

TABLE III. Ejecta properties. The columns refer to: the name of the configuration, the mass of the ejecta $M_{\rm ej}$, the kinetic energy of the ejecta $T_{\rm ej}$, the average velocity of the ejecta inside the orbital plane $\langle|v|\rangle_\rho$ (not necessarily pointing along the radial direction), the average velocity of the ejecta perpendicular to the orbital plane $\langle|v|\rangle_z$, and the average of v^2 of fluid elements inside the orbital plane $\langle\bar{v}\rangle^\rho$ and perpendicular to it $\langle\bar{v}\rangle^z$, see Paper I for more details. Results stated in the table refer to resolution R2 and results for R1 are given in brackets.

Name	$M_{\rm ej}$ $[10^{-2}M_\odot]$	$T_{\rm ej}$ $[10^{-4}]$	$\langle\|v\|\rangle_\rho$	$\langle\|v\|\rangle_z$	$\langle\bar{v}\rangle^\rho$	$\langle\bar{v}\rangle^z$
ALF2-137137^{00}	0.34 (0.20)	0.76 (0.22)	0.17 (0.12)	0.10 (0.11)	0.17 (0.12)	0.22 (0.15)
ALF2-137137$^{\uparrow\uparrow}$	0.16 (0.09)	0.18 (0.31)	0.16 (0.10)	0.05 (0.08)	0.16 (0.10)	0.14 (0.13)
ALF2-137137$^{\uparrow\downarrow}$	0.41 (0.34)	0.31 (0.49)	0.12 (0.15)	0.07 (0.10)	0.12 (0.15)	0.12 (0.16)
ALF2-137137$^{\uparrow 0}$	0.20 (0.25)	0.20 (0.20)	0.13 (0.11)	0.05 (0.07)	0.13 (0.11)	0.13 (0.13)
H4-137137^{00}	0.34 (0.06)	0.89 (0.10)	0.19 (0.13)	0.10 (0.14)	0.19 (0.13)	0.23 (0.22)
H4-137137$^{\uparrow\uparrow}$	0.20 (0.12)	0.44 (0.23)	0.15 (0.22)	0.07 (0.07)	0.16 (0.24)	0.21 (0.27)
H4-137137$^{\uparrow\downarrow}$	0.15 (0.07)	0.35 (0.12)	0.16 (0.12)	0.10 (0.10)	0.17 (0.12)	0.23 (0.20)
H4-137137$^{\uparrow 0}$	0.07 (0.06)	0.13 (0.11)	0.17 (0.14)	0.10 (0.08)	0.17 (0.14)	0.22 (0.20)
ALF2-122153^{00}	0.75 (0.97)	2.2 (2.1)	0.17 (0.09)	0.12 (0.10)	0.17 (0.09)	0.23 (0.17)
ALF2-122153$^{\uparrow\uparrow}$	0.67 (0.63)	1.4 (1.7)	0.16 (0.28)	0.08 (0.06)	0.16 (0.32)	0.20 (0.44)
ALF2-122153$^{\uparrow\downarrow}$	0.45 (0.49)	0.94 (0.74)	0.15 (0.14)	0.11 (0.09)	0.15 (0.14)	0.22 (0.18)
ALF2-122153$^{\uparrow 0}$	0.55 (1.9)	1.2 (7.8)	0.16 (0.17)	0.13 (0.13)	0.17 (0.18)	0.21 (0.20)
H4-122153^{00}	0.66 (0.88)	1.7 (1.7)	0.18 (0.15)	0.11 (0.11)	0.18 (0.16)	0.22 (0.28)
H4-122153$^{\uparrow\uparrow}$	0.78 (1.2)	1.7 (1.6)	0.18 (0.15)	0.11 (0.04)	0.18 (0.15)	0.22 (0.16)
H4-122153$^{\uparrow\downarrow}$	0.41 (0.53)	0.95 (1.1)	0.17 (0.17)	0.09 (0.11)	0.17 (0.18)	0.20 (0.22)
H4-122153$^{\uparrow 0}$	0.64 (0.40)	1.8 (1.4)	0.18 (0.25)	0.08 (0.09)	0.19 (0.28)	0.22 (0.20)
ALF2-110165^{00}	2.4 (1.5)	4.2 (2.1)	0.17 (0.15)	0.07 (0.08)	0.17 (0.15)	0.18 (0.16)
ALF2-110165$^{\uparrow\uparrow}$	2.4 (3.4)	4.2 (6.5)	0.18 (0.18)	0.04 (0.07)	0.18 (0.19)	0.18 (0.17)
ALF2-110165$^{\uparrow\downarrow}$	1.1 (0.97)	2.0 (1.5)	0.18 (0.17)	0.05 (0.05)	0.18 (0.17)	0.19 (0.18)
ALF2-110165$^{\uparrow 0}$	1.4 (1.8)	2.3 (2.5)	0.18 (0.17)	0.04 (0.06)	0.18 (0.17)	0.19 (0.17)
H4-110165^{00}	1.6 (2.0)	2.9 (2.9)	0.17 (0.16)	0.05 (0.04)	0.18 (0.16)	0.17 (0.17)
H4-110165$^{\uparrow\uparrow}$	2.7 (3.7)	4.2 (7.1)	0.17 (0.19)	0.02 (0.03)	0.17 (0.19)	0.15 (0.18)
H4-110165$^{\uparrow\downarrow}$	0.95 (1.5)	1.4 (2.5)	0.17 (0.18)	0.03 (0.05)	0.17 (0.18)	0.17 (0.18)
H4-110165$^{\uparrow 0}$	1.9 (2.0)	3.1 (3.1)	0.17 (0.17)	0.03 (0.04)	0.17 (0.17)	0.18 (0.21)

fect of the mass ratio. It is most visible for larger ejecta masses, i.e. the $q = 1.25, 1.5$ cases, and is related to the spin of the companion star (less massive NS). In a Newtonian system, mass ejection sets in once the fluid velocity is sufficiently large and the material is not bound by gravitational forces, i.e., once $v^2 > M_{\rm NS}/R_{\rm NS}$. The velocity of the fluid elements can be approximated by $v \sim v_{\rm orb} + v_\omega$. The component $v_{\rm orb}$ depends on the orbital motion and is therefore only indirectly effected by the spins. The component $v_\omega \approx \omega R_{\rm NS}$ is the speed of a fluid element in the frame moving with the center of the star. Considering the two configurations ($\uparrow\uparrow$) and ($\uparrow\downarrow$), one can approximate the fluid velocity at the points farthest away from the center of mass as $v \sim v_{\rm orb} + |v_\omega|$ for ($\uparrow\uparrow$), and as $v \sim v_{\rm orb} - |v_\omega|$ for ($\uparrow\downarrow$) configurations. The criterion $v^2 > M_{\rm NS}/R_{\rm NS}$ would be fulfilled for the former configuration but not fulfilled for the latter. This observation, although based on a Newtonian description, explains why for $q \neq 1$ the unbound mass increases with increasing χ_B. The observation that more material can be ejected for aligned configurations was also reported in [76] for eccentric encounters of NSBH systems using approximate initial data.

VI. GRAVITATIONAL WAVES

In this section we discuss spin effects on the GW. In Sec. VI A we present, for the first time, a GW phase analysis up to merger that quantifies the contributions of spin and tidal interaction in the dynamical regime covered by the simulations. We find that spin effects contribute to phase differences up to ~ 5 radians in the considered dynamical regime (for $\chi \sim 0.1$). In Sec. VI B we discuss the postmerger signal and the main emission channels. We find that aligned spin configurations have a longer lifetime before collapse and therefore influence the spectral properties of the remnant. However, resolving spin effects with current simulations in the power spectral density (PSD) of the GW signal is not possible.

Our notation follows Sec. V of Paper I, and focuses on the dominant $(2,2)$ mode of the GW strain. We often use

$$\hat{\omega} := M\omega_{22} \tag{28}$$

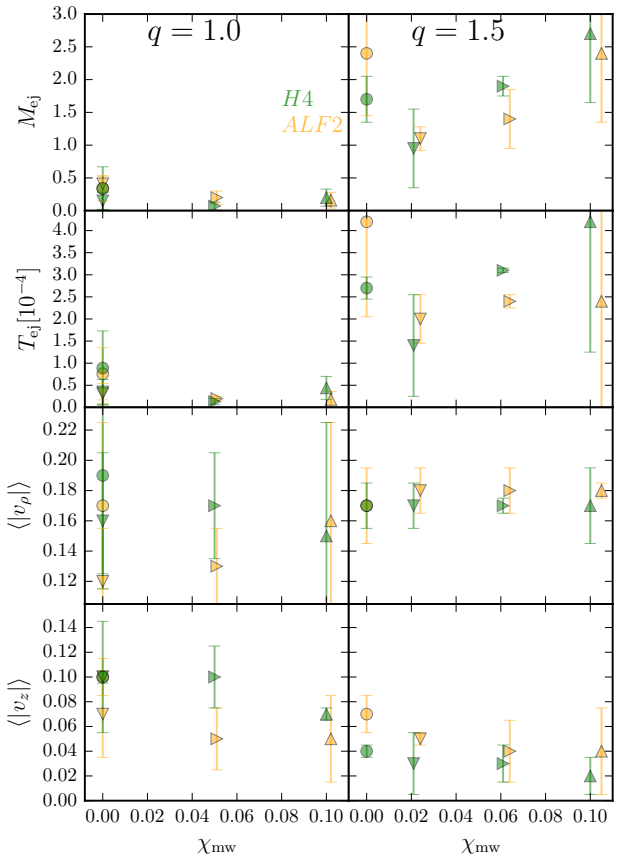

FIG. 9. Mass of the ejecta (first row), kinetic energy of the ejecta (second row), ejecta velocities inside the plane (third row) and orthogonal to it (fourth row) as a function of the spin of the configurations. Green points represent data for the H4-EOS, while orange data points correspond to ALF2. Left panels refer to mass ratio $q = 1.00$ and right panels to mass ratio $q = 1.50$. The markers characterize the spin of the configurations as in Fig. 1, where circles correspond to (00) setups, down-pointing triangles to ($\uparrow\downarrow$), right-pointing triangles to ($\uparrow$ 0), and upwards pointing triangles to ($\uparrow\uparrow$). The spin of the secondary star influences the amount of ejected material and the kinetic energy, where aligned spin leads to larger ejecta. The velocity inside the orbital plane does not depend notably on q or $\chi_{\rm eff}$, and the velocity perpendicular to the orbital plane decreases for increasing q.

for the dimensionless and mass-rescaled GW frequency. GWs are plotted versus the retarded time u. The (real part of the) waveforms is plotted in Fig. 10, as an overview of the different signals. Several important quantities are listed in Tab. IV.

A. Late-inspiral phasing

In order to analyze the phasing of the waves we proceed as follows. We first fit the quantity $\hat{\omega}(t)$ as described in App. C, eliminating this way the oscillation due the residual eccentricity in the NR data. We then integrate to obtain $\phi(t)$ and parametrize $\phi(t(\hat{\omega}))$ to obtain the phase as a function of the GW frequency. The integration introduces an arbitrary phase shift, which is set to zero at an initial frequency $\hat{\omega} = 0.04$. The phase comparison is then restricted to the frequency interval $\hat{\omega} \in [0.04, 0.11]$, which corresponds to physical GW frequencies $\sim 470-1292$ Hz.

Figure 11 summarized our results. The upper panel shows the phase of ALF2-137137$^{(00)}$ (blue) and ALF2-137137$^{(\uparrow\uparrow)}$ (red). The estimated uncertainty of the data is shown as a shaded region; note that the error bar is not symmetric. The phase of a non-spinning, equal mass BBH is included as black curve. The latter is obtained from the EOB model of [71]. In the bottom panel we show the accumulated phase due to spin and tidal interaction separately. As in the case of the energetics, we separate the spin and tidal contributions to the phase by considering the difference between the ($\uparrow\uparrow$) and (00) configuration (spin) and the difference between the (00) and the BBH configuration.

This analysis shows that tidal effects contribute to about 15 to 20 radians, accumulated in the considered frequency interval of $\hat{\omega} \in [0.04, 0.11]$. This is about 4-5 times the phase accumulated from 10 Hz to $\sim$ 470 Hz (i.e. from infinite separation up to $\hat{\omega} \sim 0.04$) estimated with PN methods [78]. Spin effects for $\chi \sim 0.1$ give an accumulated phase of ~ 5 radiants on the same frequency interval. These results are consistent with EOB predictions included as dashed lines.

Regarding the GW merger frequency (defined as the frequency at the wave's amplitude peak), Tab. IV shows that BNS systems employing a stiffer EOS and/or larger mass ratios have smaller $M\omega_{\rm mrg}$ (cf. Paper I). Spin interactions shift the merger frequency of $\Delta M\omega \sim \pm 0.005$, where the exact value depends on the mass ratio and EOS.

B. Post-merger spectra

We analyze the GW spectrum of the postmerger waveform by performing a Fourier transform of the simulation data (cf. Sec. V of Paper I). Figure 12 shows typical spectrograms of the postmerger GW. The plot highlights the continuum character of the GW frequency, which is especially evident in the cases in which the merger remnant is close to collapse. This emission mirrors the dynamics discussed in Sec. IV C 2. Due to the increasing compactness of the remnant, the GW frequency increases until the system settles to a stable state or collapses to a BH. As shown in [1, 79], however, most energy is released shortly after the formation of the HMNS. Therefore most of the power is at a frequency close to the one at the formation of the merger remnant. Spin effects are clearly distinguishable in the GW spectrum. For example, the irrotational configuration H4-137137 evolves faster to the collapse and has slightly lower frequency during the postmerger then configuration ($\uparrow\uparrow$). The frequency drift in H4-110165 is more prominent in the irrotational (00) configuration then in the ($\uparrow\uparrow$), indicating

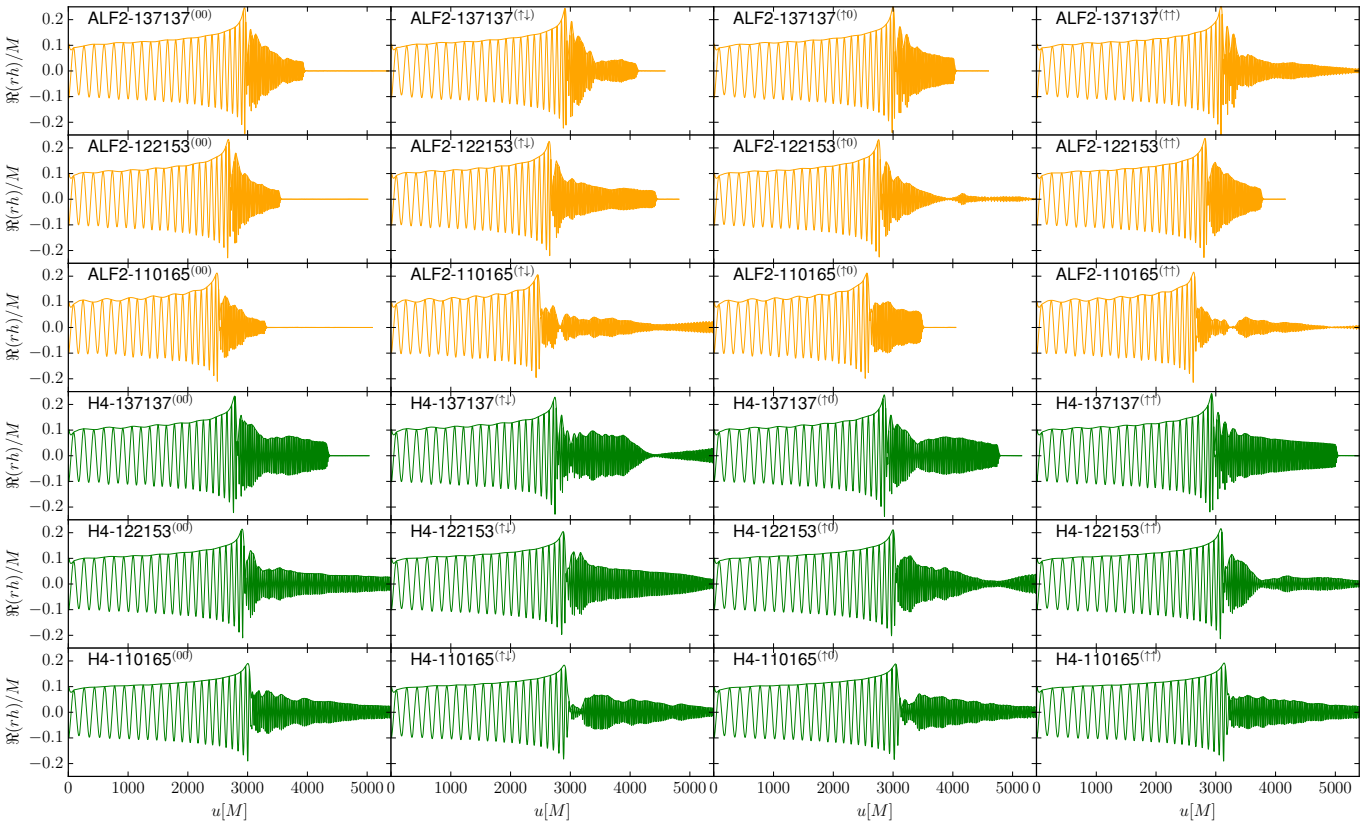

FIG. 10. Gravitational wave signal for all considered configurations employing the R2 resolution. Top panels (yellow lines) refer to the ALF2 EOS, bottom panels (green lines) refer the H4 EOS. The mass ratio from top to bottom is: $q = 1.00, q = 1.25, q = 1.50$. The columns refer to setups: (00),(↑↓), (↑ 0), (↑↑).

the remnant is closer to the threshold of radial instability (collapse).

The spectrogram plots include a horizontal blue line indicating the "peak" frequency f_2 extracted from the waveform PSD (see below). They also include as a white line the dynamical frequency $2M\Omega = 2\partial E_b/\partial \ell$ as computed in Sec. IV C 2 and as a black dashed line $M\omega_{22}$. The two frequencies remarkably agree with each other, indicating that the emission is dominated by the non-axisymmetric $m = 2$ deformation of the rotating remnant.

Figure 13 shows the spectrum of the signal for two exemplary cases. Some broad peaks can be identified in the PSD, and we report for completeness some peak frequencies in Tab. IV. As described in Paper I, the frequencies f_1, f_2, f_3 refer to the dominant frequencies of the $(2,1)$,$(2,2)$,$(3,3)$-modes, respectively. Secondary peaks f_s are also present, see [80–83] for a discussion. As we discussed in Paper I, the f_s peak at a frequency close to the merger frequency is basically absent for high mass ratio BNS, while a secondary peak with slightly lower frequency as the f_2-frequency becomes visible. Here we find that the secondary peak close to the merger frequency is enhanced for aligned spin configurations.

In Ref. [25] we reported a shift of the f_2 frequency of about ~ 200 Hz due to the spin of the NSs. Those simulations used higher resolutions than the ones presented here, but were restricted to a simple $\Gamma = 2$ EOS. Ref. [30] found that for more realistic EOS but under the assumption of conformal flatness the frequency shift is smaller. In our new data we cannot clearly resolve frequency shifts of $\lesssim 200$ Hz, which is then to be considered an upper limit for spin effects in BNS with the employed EOSs and spins $\chi \lesssim 0.1$ [see also the discussion in Sec. IV C 2]. Nevertheless, we find in agreement with [25] that aligned spin configurations have higher peak frequencies f_2. For our setups the shift is only on the order of $\lesssim 50$Hz and thus not resolved properly. Longer and higher resolved simulations will be needed for a further investigation of the f_2-shift.

VII. EM COUNTERPARTS

Let us now discuss spin effects in possible EM counterparts in the infrared and radio band generated from the mass ejecta. As a consequence of the results about the dynamical ejecta, we find that spins effects are subdominant with respect mass-ratio effect, and more relevant the larger the unbound mass is, i.e. for large q. However, we identify a clear trend: aligned spins increase the luminosity of the kilonovae and the radio fluency of the radio

TABLE IV. Gravitational waveform quantities. The columns refer to: the name of the configuration, the number of orbits up to merger, the dimensionless frequency at merger $M\omega_{mrg}$, the merger frequency in kHz, the dominant frequencies during the post merger stage f_1, f_2, f_3 stated in kHz and extracted from the (2,1),(2,2),(3,3)-mode. Results stated in the table refer to resolution R2 and results for R1 are given in brackets.

Name	$N_{\rm orb}$	$M\omega_{\rm mrg}$	$f_{\rm mrg}$	f_1	f_2	f_3
ALF2-137137$^{(00)}$	11.5 (11.0)	0.144 (0.142)	1.69 (1.67)	1.55 (1.46)	2.80 (2.77)	4.30 (4.06)
ALF2-137137$^{(\uparrow\downarrow)}$	11.3 (10.9)	0.141 (0.138)	1.66 (1.62)	1.42 (1.36)	2.77 (2.65)	4.13 (3.78)
ALF2-137137$^{(\uparrow 0)}$	11.7 (11.3)	0.147 (0.142)	1.73 (1.67)	1.46 (1.35)	2.81 (2.63)	4.08 (3.84)
ALF2-137137$^{(\uparrow\uparrow)}$	12.0 (11.5)	0.147 (0.144)	1.73 (1.69)	1.45 (1.43)	2.75 (2.75)	4.17 (3.99)
H4-137137$^{(00)}$	10.4 (10.5)	0.133 (0.127)	1.56 (1.49)	1.27 (1.38)	2.50 (2.58)	3.74 (3.84)
H4-137137$^{(\uparrow\downarrow)}$	10.6 (10.3)	0.128 (0.126)	1.50 (1.48)	1.38 (1.37)	2.58 (2.61)	4.50 (3.97)
H4-137137$^{(\uparrow 0)}$	11.0 (10.8)	0.133 (0.128)	1.56 (1.50)	1.28 (1.35)	2.50 (2.55)	4.30 (4.23)
H4-137137$^{(\uparrow\uparrow)}$	11.3 (11.1)	0.136 (0.134)	1.59 (1.57)	1.36 (1.36)	2.54 (2.51)	-
ALF2-122153$^{(00)}$	10.6 (10.1)	0.133 (0.131)	1.56 (1.57)	1.42 (1.44)	2.72 (2.68)	4.11 (4.13)
ALF2-122153$^{(\uparrow\downarrow)}$	10.4 (9.9)	0.126 (0.123)	1.48 (1.45)	1.46 (1.42)	2.73 (2.74)	3.86 (4.17)
ALF2-122153$^{(\uparrow 0)}$	10.9 (10.4)	0.133 (0.130)	1.56 (1.53)	1.45 (1.38)	2.70 (2.71)	4.33 (4.16)
ALF2-122153$^{(\uparrow\uparrow)}$	11.2 (10.7)	0.135 (0.133)	1.58 (1.56)	1.43 (1.40)	2.75 (2.70)	4.22 (4.10)
H4-122153$^{(00)}$	10.7 (10.3)	0.114 (0.115)	1.34 (1.35)	1.28 (1.24)	2.42 (2.38)	3.78 (3.70)
H4-122153$^{(\uparrow\downarrow)}$	10.7 (10.3)	0.108 (0.106)	1.27 (1.25)	1.38 (1.29)	2.49 (2.47)	4.26 (3.95)
H4-122153$^{(\uparrow 0)}$	11.2 (10.9)	0.112 (0.111)	1.32 (1.30)	1.29 (1.28)	2.51 (2.47)	4.07 (4.12)
H4-122153$^{(\uparrow\uparrow)}$	11.6 (11.2)	0.115 (0.114)	1.35 (1.34)	1.27 (1.29)	2.49 (2.49)	3.70 (3.79)
ALF2-110165$^{(00)}$	9.9 (9.6)	0.119 (0.118)	1.40 (1.39)	1.45 (1.32)	2.74 (2.74)	4.17 (4.06)
ALF2-110165$^{(\uparrow\downarrow)}$	9.7 (9.3)	0.114 (0.113)	1.34 (1.33)	1.44 (1.40)	2.82 (2.79)	4.20 (4.24)
ALF2-110165$^{(\uparrow 0)}$	10.3 (9.7)	0.118 (0.116)	1.39 (1.36)	1.43 (1.33)	2.83 (2.69)	4.05 (4.00)
ALF2-110165$^{(\uparrow\uparrow)}$	10.6 (10.0)	0.121 (0.120)	1.42 (1.41)	1.42 (1.41)	2.80 (2.80)	4.18 (4.24)
H4-110165$^{(00)}$	11.0 (10.7)	0.100 (0.098)	1.17 (1.15)	1.27 (1.24)	2.48 (2.43)	3.83 (3.54)
H4-110165$^{(\uparrow\downarrow)}$	10.6 (10.1)	0.095 (0.095)	1.12 (1.12)	1.29 (1.24)	2.58 (2.50)	3.98 (3.80)
H4-110165$^{(\uparrow 0)}$	11.2 (10.8)	0.098 (0.097)	1.15 (1.14)	1.29 (1.24)	2.56 (2.53)	3.98 (3.77)
H4-110165$^{(\uparrow\uparrow)}$	11.6 (11.2)	0.100 (0.099)	1.17 (1.16)	1.28 (1.27)	2.54 (2.54)	3.93 (3.78)

flares and, therefore, favor the detection of EM counterparts.

As in Paper I we use the analytical model of [84] to estimate the peak luminosity, time, and temperature of the marcronovae produced by the ejecta. We also use the model of [12] to describe radio flares peak fluxes. Our results are summarized in Tab. V, Fig. 14, and Fig. 15.

As pointed out with previous studies an increasing mass ratio delays the luminosity peak of the kilonovae for few days, but leads to an overall larger peak luminosity. Also, the temperature at peak luminosity decreases for larger mass ratios. The effect of the spins is less strong, but because of the larger ejecta mass for systems for which the secondary star has spin aligned to the orbital angular momentum we find a trend towards delayed peaks, increasing luminosity, and decreasing temperature. This effect is clearly present for larger mass ratios, see Fig. 14.

We present the bolometric luminosities for the expected kilonova. The lightcurves are computed following the approach of [85, 86]. Figure 16 shows the bolometric luminosity for the H4-165110 setups considering different spin configurations. Because of the larger ejecta mass for the ($\uparrow\uparrow$) configuration the bolometric luminosity is larger than for the other setups. Contrary when the secondary star has antialigned spin the bolometric luminosity is about a factor of ~ 2 smaller than for the aligned setup.

Considering the radio flares, we find that systems with a larger mass ratio are more likely to be detectable than equal mass setups, Fig. 15. The fluency and the peak time increase with increasing mass ratio. Our results suggest that in cases where the less massive star has spin aligned to the orbital angular momentum the radio fluency increases and happens at later times.

For a more quantitative analysis higher resolution simulations and better models estimating the kilonova and radio burst properties are needed. Note also that, since our simulations are based on simulations not including microphysics and on simplified models, further simulations are needed to check our results.

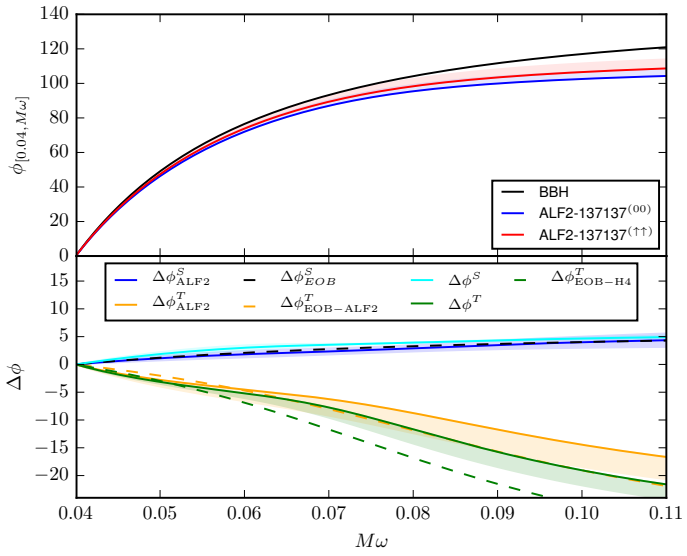

FIG. 11. Top panel: $\phi(\hat{\omega})$ accumulated in $\hat{\omega} \in [0.04, 0.11]$ for ALF2-137137$^{(00)}$ (blue), ALF2-137137$^{(\uparrow\uparrow)}$ (red), and a non-spinning, equal mass BBH setup (black). Bottom panel: individual contributions $\Delta\phi(\hat{\omega})$. We include tidal effects for ALF2 (orange) and H4 (green) EOS, as well as spin effects for ALF2 (blue) and H4 (cyan). We also include estimates from the EOB models of [71] for the spinning contribution and [77] for the tidal contribution as dashed lines.

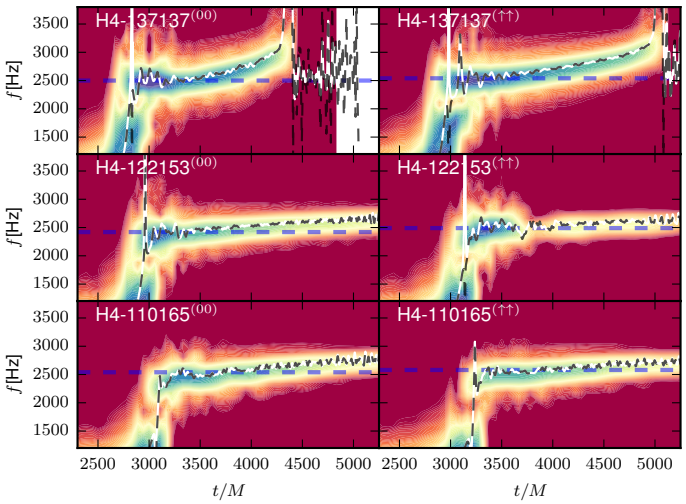

FIG. 12. Spectrogram of the GW signal for simulations with H4 EOS and resolution R2. The spectrogram only considers the dominant (2,2) mode. Horizontal blue dashed lines refer to the f_2 frequency extracted from the entire postmerger GW signal. Black dashed lines refer to the frequency of the (2,2)-mode and white lines refer to the frequency extracted from the binding energy $\partial_\ell E$ (Fig. 8). The spectrograms show the last part of the inspiral signal (left bottom corners of the spectrograms) and evolution of the HMNS.

VIII. SUMMARY

In this article we studied the effect of the stars' rotation on equal and unequal mass binary neutron star mergers dynamics. Our analysis provides a basis for future models of spin effects in gravitational waves and electromagnetic emission. Combined with Paper I ([1]) this work is one of the most complete investigations of the binary neutron star parameter space available to date.

Our findings are summarized in what follows.

Energetics: We have considered gauge-invariant binding energy curves for both fixed orbital angular momentum $E_b(\ell)$ and fixed orbital frequency $E_b(x)$. The former are useful to understand the effect of individual terms in the Hamiltonian; the latter are directly linked to the GW phase analysis (see below).

Our new analysis of the energetics up to merger indicates that, although the main spin effect is due to spin-orbit (SO) interactions [25], also spin-spin interaction might play a role in the very last stage of the merger. In particular, we argue that a self-coupling of the NS spin (S_A^2 (14)) caused by quadrupole deformation of the star due to its intrinsic rotation contributes during the last orbits with an attractive effect opposed to the repulsive effect of the SO interaction [87]. This illustrates the importance of including also spin-spin effects in analytical models of BNS, and poses the challenge of resolving such effects in NR simulations.

We note that the current best analytical representation of the SO Hamiltonian (the effective-one-body model, EOB) shows some significant deviation from the NR data at small separations, see Fig. 4. Curiously, comparing the EOB analytical SO model with NR data that include also the S^2 interaction, we find an effective closer agreement between the two, Fig. 5.

We have used energetics and the dynamical frequency $\Omega = M^{-1}\partial E_b/\partial\ell$ also to analyze the postmerger dynamics. Spin effects are clearly visible in cases in which the merger remnant collapses to black hole, Fig. 8. Spins aligned to orbital angular momentum increase the angular momentum support of the remnant, therefore, collapse happens at later times and at smaller values of ℓ. Spin effects on the frequency evolution of more stable merger remnant are small and difficult to resolve. The Ω analysis also shows that in large-mass ratio BNS ($q \gtrsim 1.5$), the rotational frequency Ω has a sharp increase right after merger due to the collision of the companion's core with the primary star (Fig. 8 bottom right panel). This fact was unnoticed in Paper I where we did not inspect energetics.

Mass ejection: Spin effects in dynamical ejecta are clearly observed in unequal mass BNS (and with large mass ratios, $q \sim 1.3 - 1.5$), in which mass ejection originates from the tidal tail for the companion. Spin aligned to the orbital angular momentum favors the amount of ejected mass because the additional angular momentum contributes to unbinding a larger fraction of fluid elements. This effect is mostly dependent on the spin of the companion.

Gravitational Waves: We presented the first analysis of spin effects in the GW phase up to merger. Spin effects

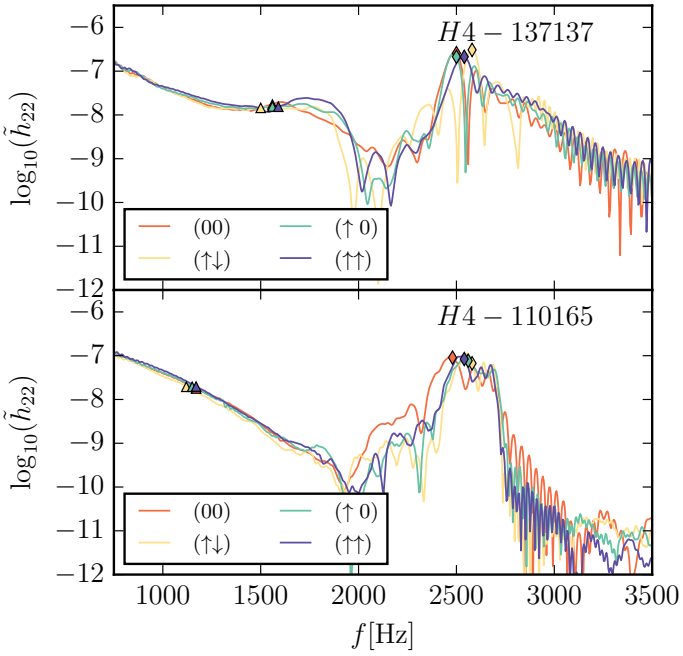

FIG. 13. PSD for the H4-137137 (upper panel) and H4-110165 (lower panel) setups. We mark the merger frequency with triangles and the postmerger peak frequency f_2 as diamonds.

contribute to phase differences up to ~ 5 radians in the considered dynamical regime (and for $\chi \sim 0.1$). This dephasing should be compared with the ~ 20 radiants due to tidal effects accumulated to the BNS merger (with respect a BBH). The hierarchy of these effects on the phase mirrors what is observed in the energetics $E_b(x)$, Fig. 6. Neglecting spin effects would bias the determination of tidal parameters in GW observations, e.g. [33]. Mainly as a consequence of spin-orbit interactions, the merger GW frequency of CRV BNS shift to higher (lower) frequencies then irrotational BNS if a NS has aligned (antialigned) spin to the orbital angular momentum.

The Fourier analysis of the postmerger signal indicates that spin effects are visible in the GW spectrum (cf. Fig. 13 and 12). Some differences in the GW frequency evolution are observed in cases the additional angular momentum support due to aligned spins stabilizes the merger remnant for a longer time period (cf. discussion on spin effects on dynamics). Our simulations suggest that if a BNS has spin aligned to the angular momentum the spectrum is slightly shifted to higher frequencies up to ~ 50 Hz (for dimensionless spins $\chi \lesssim 0.1$), but more accurate simulations with longer postmerger evolutions will be needed to resolve the shift properly. Furthermore, we see an effect of the spin on the secondary peak frequencies, where aligned configurations increase the enhance a secondary peak shortly after the merger frequency.

Electromagnetic counterparts: For the considered spin magnitudes the spin effects on the kilonovae and radio flare properties is subdominant with respect to the mass ratio and the EOS. Spin effects are more prominent for larger ejecta masses, where spin aligned (antialigned) with the orbital angular momentum increases (decreases) the luminosity of the kilonovae and also increases (decreases) the radio fluency of the radio flares. Overall we find that aligned spin BNS in combination with larger mass ratios favor bright electromagnetic counterparts.

TABLE V. Electromagnetic Counterparts. The columns refer to: the name of the configuration, the time in which the peak in the near infrared occurs $t_{\rm peak}$, the corresponding peak luminosity $L_{\rm peak}$, the temperature at this time $T_{\rm peak}$, the time of peak in the radio band $t^{\rm rad}_{\rm peak}$, and the corresponding radio fluence. As in other tables, we present results for R2 and in brackets resolutions for R1.

Name	$t_{\rm peak}$ [days]	$L_{\rm peak}$ [$10^{40}\frac{\rm erg}{\rm s}$]	$T_{\rm peak}$ [10^3 K]	$t^{\rm rad}_{\rm peak}$ [years]	$F^{\nu{\rm rad}}_{\rm peak}$ [μJy]
ALF2-137137$^{(00)}$	2.0 (1.8)	2.6 (1.9)	2.5 (2.7)	6.4 (6.1)	41 (7)
ALF2-137137$^{(\uparrow\downarrow)}$	2.7 (2.2)	2.3 (2.5)	2.5 (2.5)	8.4 (6.7)	8 (20)
ALF2-137137$^{(\uparrow 0)}$	1.8 (2.1)	1.8 (1.8)	2.8 (2.7)	7.2 (8.1)	5 (4)
ALF2-137137$^{(\uparrow\uparrow)}$	1.5 (1.3)	1.8 (1.2)	2.8 (3.2)	5.2 (10.0)	7 (6)
H4-137137$^{(00)}$	1.9 (0.9)	2.8 (1.4)	2.5 (3.3)	5.9 (3.5)	58 (5)
H4-137137$^{(\uparrow\downarrow)}$	1.4 (1.0)	2.0 (1.3)	2.8 (3.3)	5.0 (4.9)	19 (4)
H4-137137$^{(\uparrow 0)}$	0.9 (1.0)	1.5 (1.3)	3.2 (3.3)	3.7 (4.9)	7 (4)
H4-137137$^{(\uparrow\uparrow)}$	1.7 (1.1)	2.0 (2.0)	2.7 (2.9)	6.8 (3.3)	17 (18)
ALF2-122153$^{(00)}$	2.9 (4.2)	3.7 (2.9)	2.2 (2.2)	8.0 (17.6)	139 (46)
ALF2-122153$^{(\uparrow\downarrow)}$	2.4 (2.7)	2.8 (2.7)	2.4 (2.4)	7.6 (8.4)	44 (27)
ALF2-122153$^{(\uparrow 0)}$	2.5 (4.6)	3.3 (5.2)	2.3 (1.9)	6.9 (11.9)	74 (516)
ALF2-122153$^{(\uparrow\uparrow)}$	3.0 (2.3)	3.2 (4.2)	2.2 (2.2)	8.9 (4.5)	64 (215)
H4-122153$^{(00)}$	2.7 (3.4)	3.5 (3.5)	2.2 (2.1)	7.3 (9.6)	105 (74)
H4-122153$^{(\uparrow\downarrow)}$	2.3 (2.5)	2.8 (3.1)	2.4 (2.3)	7.2 (6.9)	48 (61)
H4-122153$^{(\uparrow 0)}$	2.8 (1.9)	3.3 (3.5)	2.2 (2.3)	8.3 (4.6)	99 (149)
H4-122153$^{(\uparrow\uparrow)}$	3.0 (4.3)	3.7 (3.5)	2.1 (2.1)	7.4 (12.0)	108 (52)
ALF2-110165$^{(00)}$	5.6 (4.6)	5.0 (4.1)	1.8 (2.0)	12.8 (11.4)	190 (83)
ALF2-110165$^{(\uparrow\downarrow)}$	3.8 (3.6)	3.9 (3.6)	2.0 (2.1)	9.7 (9.5)	96 (65)
ALF2-110165$^{(\uparrow 0)}$	4.3 (4.9)	4.1 (4.4)	2.0 (1.9)	10.6 (11.5)	106 (104)
ALF2-110165$^{(\uparrow\uparrow)}$	5.5 (6.5)	5.0 (6.0)	1.8 (1.7)	12.5 (12.9)	198 (352)
H4-110165$^{(00)}$	4.6 (5.4)	4.4 (4.5)	1.9 (1.9)	11.2 (12.9)	133 (109)
H4-110165$^{(\uparrow\downarrow)}$	3.7 (4.4)	3.4 (4.3)	2.1 (2.0)	10.2 (10.6)	53 (116)
H4-110165$^{(\uparrow 0)}$	5.1 (5.3)	4.5 (4.5)	1.9 (1.9)	12.5 (12.7)	126 (124)
H4-110165$^{(\uparrow\uparrow)}$	6.2 (6.9)	5.0 (6.0)	1.8 (1.7)	14.5 (14.3)	160 (352)

ACKNOWLEDGMENTS

It is a pleasure to thank Bernd Brügmann, Roland Haas, Tanja Hinderer, Nathan K. Johnson-McDaniel, Harald Pfeiffer, Jan Steinhoff, Justin Vines for helpful discussions. We are very thankful to Alessandro Nagar for providing us with EOB $E_b(\ell)$ curves and to Serguei Ossokine for providing us with the NR black holes binary $E_b(\ell)$. We thank David Radice for comments improving the manuscript. W.T. was supported by the National Science Foundation under grant PHY-1305387. Computations where performed on SuperMUC at the LRZ (Mu-

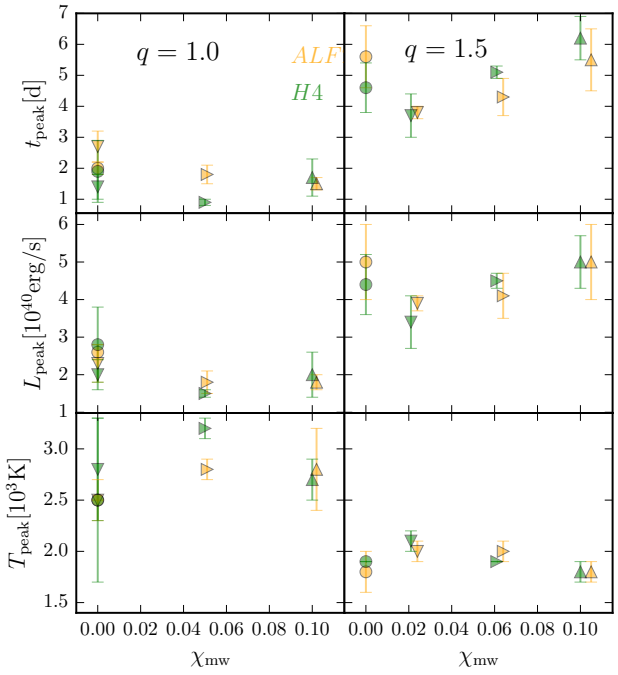

FIG. 14. Peak time $t_{\rm peak}$ (top panel), peak luminosity $L_{\rm peak}$ (middle panel), and peak temperature $T_{\rm peak}$ (bottom panel) of marcronovae produced by the BNS mergers considered in this article as a function of the effective spin $\chi_{\rm eff}$. We mark different EOS with different colors: green (H4) and orange (ALF2). Different markers refer to different spin configurations, see Fig. 1.

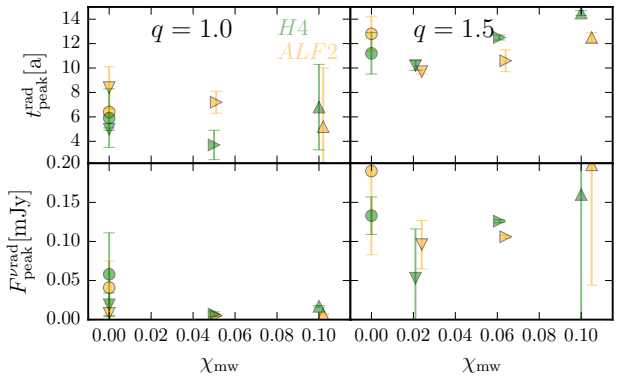

FIG. 15. Peak time in the radio band $t^{\rm rad}_{\rm peak}$ (top panel) and corresponding radio fluence $F^{\nu{\rm rad}}_{\rm peak}$ (bottom panel), as a function of the effective spin $\chi_{\rm eff}$. We mark different EOS with different colors: green (H4) and orange (ALF2). Different markers refer to different spin configurations, see Fig. 1.

nich) under the project number pr48pu, Jureca (Jülich) under the project number HPO21, Stampede (Texas, XSEDE allocation - TG-PHY140019), Marconi (ISCRA-B) under the project number HP10BMAB71.

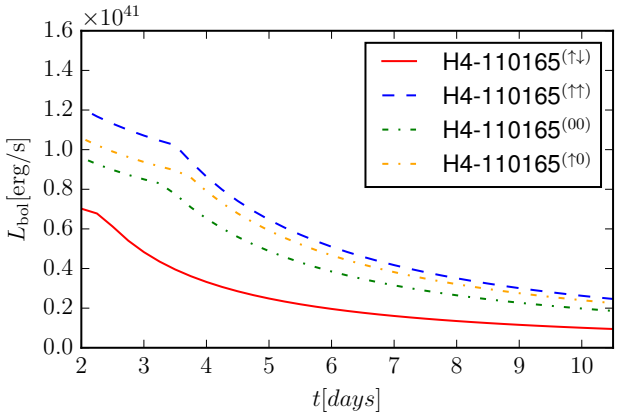

FIG. 16. Bolometric luminosity for the H4-110165 setups with different spin orientations. The luminosities are computed following the approach of [85].

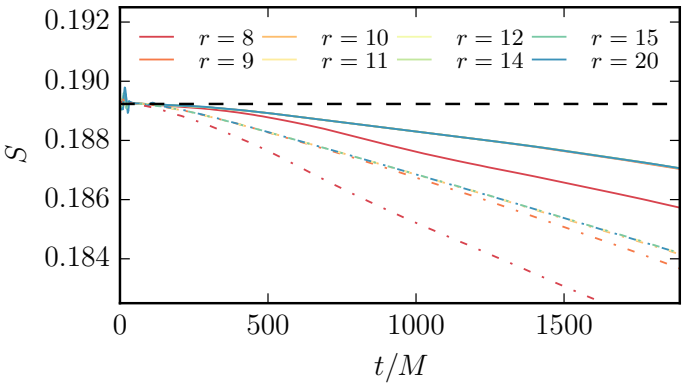

FIG. 17. Quasi-local spin measure, Eq. (1), for a single rotating NS in equilibrium. The NS has similar mass and spin to the components of H4−137137$^{(\uparrow\uparrow)}$. Different colors refer to different coordinate radii, where solid lines represent results for resolution R2 and dashed lines for resolution R1. The ADM angular momentum measured with SGRID is given as a black dashed line.

Appendix A: Quasi-local spin measures for isolated rotating NS

In this appendix we evaluate the accuracy of the quasi-local measurements for isolated rotating stars in equilibrium. Equation (1) converges to the ADM angular momentum for $r_S \to \infty$. This test is important to support the interpretation of Eq. (1) as a "spin measure".

Figure 17 shows our findings for a single NS with the H4 EOS, a mass of $M = 1.375$ and a dimensionless spin of $\chi = 0.10$. We compute Eq. (1) for different coordinate radii centered around the minimum of the lapse. The black dashed line marks the ADM value computed by the SGRID solver, i.e. at $t = 0$. The approximation of the ADM angular momentum by Eq. (1) improves for larger radii up to a point where all material is covered within the coordinate sphere. The continuous decrease of the spin measure is caused by numerical dissipation, and

it improves at higher resolution, cf. difference between solid lines (resolution R2) and dash-lines (resolution R1). This test for a single NS supports our observation that the main inaccuracies of Eq. (1) for BNS is caused by the orbital motion of the two stars and our choice of the integration surface.

Appendix B: Post-Newtonian expressions for $E(\ell)$ and $E(x)$

We report for completeness the expressions for the 3.5PN contributions to $E(\ell)$ and $E(x)$ used in Sec. IV. We discard cubic terms in the spin and refer to [73] for more details. The 4PN binding energy including higher spin terms can be found in e.g. [88, 89].

The SO contribution is

$$E_{SO}(x) = \nu x^{5/2}\left(\bar{S}^A + \bar{S}^B\right)\left(-\frac{4}{3} + x\left(\frac{31\nu}{18} - 4\right) - x^2\left(\frac{7\nu^2}{12} - \frac{211\nu}{8} + \frac{27}{2}\right)\right) + \\ + \nu x^{5/2}\left(\frac{\bar{S}^A}{q} + \bar{S}^B q\right)\left(-1 + x\left(\frac{5\nu}{3} - \frac{3}{2}\right) - x^2\left(\frac{5\nu^2}{8} - \frac{39\nu}{2} + \frac{27}{8}\right)\right), \tag{B1}$$

$$E_{SO}(\ell) = \frac{\nu(\bar{S}^A + \bar{S}^B)}{\ell^5}\left(2 + \frac{1}{\ell^2}\left(\frac{3\nu}{8} + 18\right) + \frac{1}{\ell^4}\left(\frac{5\nu^2}{16} - 27\nu + 162\right)\right) \\ + \frac{\nu(\bar{S}^A q^{-1} + \frac{\bar{S}^B}{q})}{\ell^5}\left(\frac{3}{2} + \frac{99}{8\ell^2} - \frac{1}{\ell^4}\left(\frac{195\nu}{8} - \frac{1701}{16}\right)\right). \tag{B2}$$

The SS S^2 contribution is

$$E_{S^2}(x) = \nu(\bar{S}^A)^2 x^3\left(q^{-1}\left(\frac{C_{Q_A}}{2} + \frac{5x}{6}(\nu - 3) + \frac{5xC_{Q_A}}{4}(\nu + 1)\right) + \nu x\left(\frac{25}{18} + \frac{5C_{Q_A}}{3}\right)\right) + (A \leftrightarrow B), \tag{B3}$$

$$E_{S^2}(\ell) = -\frac{\nu(\bar{S}^A)^2}{\ell^6}\left(q^{-1}\left(\frac{C_{Q_A}}{2} + \frac{1}{8\ell^2}(54\nu + 63) + \frac{C_{Q_A}}{4\ell^2}(5\nu + 21)\right) + \frac{\nu}{\ell^2}\left(\frac{65}{8} + C_{Q_A}\right)\right) + (A \leftrightarrow B), \tag{B4}$$

with $C_{Q_A} \approx a\chi_A^2 M_A^3$ describing the quadrupole deformation due to spin and a depending on the EOS ranging from $\sim 1 - 10$, see e.g. [87]. The SS $S \leftrightarrow S$ contribution is

$$E_{S\leftrightarrow S}(x) = \nu\frac{\bar{S}^A\bar{S}^{B\,3}}{x}\left(1 + x\left(\frac{5\nu}{18} + \frac{5}{6}\right)\right), \tag{B5}$$

$$E_{S\leftrightarrow S}(\ell) = -\nu\frac{\bar{S}^A\bar{S}^B}{\ell^6}\left(1 + \frac{1}{\ell^2}\left(\frac{13\nu}{4} + \frac{69}{2}\right)\right). \tag{B6}$$

Appendix C: Fits of $\hat{\omega}$ and $Q_{\hat{\omega}}$ phasing

The phasing analysis of numerical data is usually complicated by residual eccentricity and numerical noise. To minimize these effects we fit $\hat{\omega}(t)$ with the following template inspired by the PN theory

$$\hat{\omega}(t) = \frac{1}{4}x\left(1 + \sum_{n=1}^{N} c_n x^n\right), \tag{C1}$$

where $x = \tau^{-3/8}$ and $\tau = ([\nu(t_c - t)/5]^2 + d^2)^{1/2}$. The quantities t_c and d are determined by the fit, using as an initial guess for t_c the merger time and $d = (4\hat{\omega}_{\rm peak})^{-8/3}$, where $\hat{\omega}_{\rm peak}$ is the value of the peak of $\hat{\omega}$, right after the wave's amplitude peak. We fit on a frequency interval $I_\omega = [\hat{\omega}_1, \hat{\omega}_2]$ for $N = 6$. The fit result for an exemplary case is presented in Fig. 18. The residuals are flat and show that an eccentricity $\sim 10^{-2}$ is "filtered out".

In this appendix we consider a second phasing analysis based on the quantity

$$Q_{\hat{\omega}} = \frac{\hat{\omega}^2}{\dot{\hat{\omega}}}, \tag{C2}$$

where $\hat{\omega}(u/M)$ and the time derivative is taken with respect the mass-rescaled dimensionless retarded time. In PN theory $Q_{\hat{\omega}}$ is an adiabatic parameter that characterizes the validity of the stationary phase approximation e.g. [90]. The phase accumulated between two different frequencies is given by

$$\Delta\phi(\hat{\omega}_1, \hat{\omega}_2) = \int_{\hat{\omega}_1}^{\hat{\omega}_2} Q_{\hat{\omega}}\, d\log(\hat{\omega}). \tag{C3}$$

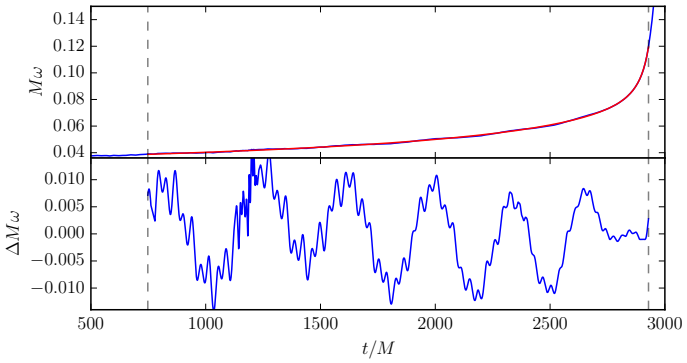

FIG. 18. Example of frequency fit with template (C1). The fitting interval is $I_\omega = [0.039, 0.129]$, covering about 18 cycles of a total of 23. The GW frequency at $u_{\rm mrg}$ is ~ 0.144 (vertical line). Data refer to ALF2 $q = 1$ $M = 2.75$ and no spin.

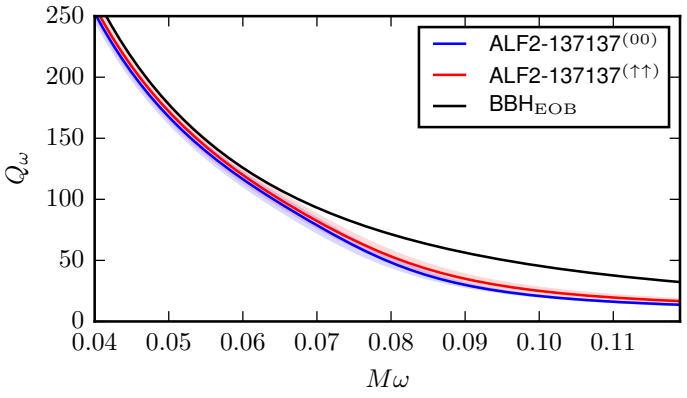

FIG. 19. $Q_{\hat\omega}(\omega)$ plot for the irrotational (blue) and $(\uparrow\uparrow)$ configuration (red) employing the ALF2 EOS. $Q_{\hat\omega}$ is computed as described in App. C. We show as shaded regions the difference between different resolutions $|Q^{R2}_{\hat\omega} - Q^{R1}_{\hat\omega}|$. As a black line we include $Q_{\hat\omega}$ for a non-spinning, equal-mass BBH setup obtained from the EOB code [71].

The use of Q_ω allows to perform, in principle, a phasing analysis without manually align the waveforms in time and phase. In practice, however, the calculation of this quantity is delicate due to numerical inaccuracies, and a fit to the frequency needs to be used. We verified as a further check of our fitting procedure that the total phase computed with Eq. (C3) is compatible with the phase of the raw data.

In Fig. 19 we present $Q_{\hat\omega}(\hat\omega)$ for ALF2-137137$^{(00)}$ (blue) and ALF2-137137$^{(\uparrow\uparrow)}$ (red) and a nonspinning $q = 1$ BBH (black, again given by the EOB model of [71]). We show as a shaded region an uncertainty estimated as $|Q^{R2}_{\hat\omega} - Q^{R1}_{\hat\omega}|$. The largest difference between $Q_{\hat\omega}(\hat\omega)$ curves is due to tidal effects, and amount to $\Delta Q^{T}_{\hat\omega} \sim 15 - 35$. From Eq. (C3) we obtain a dephasing compatible with the analysis of Sec. VI A. Spin effects for $\chi \sim 0.1$ and aligned spin give a shift of about $\Delta Q^{Spin}_{\hat\omega} \approx 5$; i.e. for a given frequency, aligned spins setups have a smaller $\dot{\hat\omega}$. Although difficult to resolve in this plot, both tidal and spin effects are in agreement with predictions from the EOB model in the considered frequency interval. A quantitative $Q_{\hat\omega}$ analysis beyond the results stated above will need future simulations with lower eccentricities and higher resolutions.

[1] T. Dietrich, M. Ujevic, W. Tichy, S. Bernuzzi, and B. Bruegmann, (2016), arXiv:1607.06636 [gr-qc].
[2] B. P. Abbott *et al.* (Virgo, LIGO Scientific), Phys. Rev. Lett. **116**, 061102 (2016), arXiv:1602.03837 [gr-qc].
[3] B. Abbott *et al.* (Virgo, LIGO Scientific), Phys. Rev. Lett. **116**, 241103 (2016), arXiv:1606.04855 [gr-qc].
[4] J. Aasi *et al.* (LIGO Scientific Collaboration, Virgo Collaboration), Living Rev. Relativity **19**, 1 (2016), arXiv:1304.0670 [gr-qc].
[5] B. Paczynski, Astrophys. J. **308**, L43 (1986).
[6] D. Eichler, M. Livio, T. Piran, and D. N. Schramm, Nature **340**, 126 (1989).
[7] A. M. Soderberg *et al.*, Astrophys. J. **650**, 261 (2006), arXiv:astro-ph/0601455 [astro-ph].
[8] N. Tanvir, A. Levan, A. Fruchter, J. Hjorth, K. Wiersema, *et al.*, Nature **500**, 547 (2013), arXiv:1306.4971 [astro-ph.HE].
[9] B. Yang, Z.-P. Jin, X. Li, S. Covino, X.-Z. Zheng, K. Hotokezaka, Y.-Z. Fan, T. Piran, and D.-M. Wei, Nature Commun. **6**, 7323 (2015), arXiv:1503.07761 [astro-ph.HE].
[10] Z.-P. Jin, K. Hotokezaka, X. Li, M. Tanaka, P. D'Avanzo, Y.-Z. Fan, S. Covino, D.-M. Wei, and T. Piran, (2016), arXiv:1603.07869 [astro-ph.HE].
[11] B. D. Metzger, (2016), arXiv:1610.09381 [astro-ph.HE].
[12] E. Nakar and T. Piran, Nature **478**, 82 (2011), arXiv:1102.1020 [astro-ph.HE].
[13] B. Kiziltan, A. Kottas, M. De Yoreo, and S. E. Thorsett, Astrophys.J. **778**, 66 (2013), arXiv:1309.6635 [astro-ph.SR].
[14] J. M. Lattimer, Ann. Rev. Nucl. Part. Sci. **62**, 485 (2012), arXiv:1305.3510 [nucl-th].
[15] M. Dominik, K. Belczynski, C. Fryer, D. E. Holz, E. Berti, T. Bulik, I. Mandel, and R. O'Shaughnessy, Astrophys. J. **759**, 52 (2012), arXiv:1202.4901 [astro-ph.HE].
[16] T. Dietrich, N. Moldenhauer, N. K. Johnson-McDaniel, S. Bernuzzi, C. M. Markakis, B. Brügmann,

and W. Tichy, Phys. Rev. D **91**, 124007 (2015), arXiv:1507.07100 [gr-qc].
[17] J. G. Martinez, K. Stovall, P. C. C. Freire, J. S. Deneva, F. A. Jenet, M. A. McLaughlin, M. Bagchi, S. D. Bates, and A. Ridolfi, Astrophys. J. **812**, 143 (2015), arXiv:1509.08805 [astro-ph.HE].
[18] P. Lazarus *et al.*, (2016), arXiv:1608.08211 [astro-ph.HE].
[19] D. R. Lorimer, Living Rev. Rel. **11**, 8 (2008), arXiv:0811.0762 [astro-ph].
[20] M. Burgay, N. D'Amico, A. Possenti, R. Manchester, A. Lyne, *et al.*, Nature **426**, 531 (2003), arXiv:astro-ph/0312071 [astro-ph].
[21] F. Verbunt and P. C. C. Freire, Astron. Astrophys. **561**, A11 (2014), arXiv:1310.4669 [astro-ph.SR].
[22] M. J. Benacquista and J. M. B. Downing, Living Rev. Relativity **16**, 4 (2013), arXiv:1110.4423 [astro-ph.SR].
[23] W. Tichy, Phys.Rev. **D84**, 024041 (2011), arXiv:1107.1440 [gr-qc].
[24] W. Tichy, Phys. Rev. D **86**, 064024 (2012), arXiv:1209.5336 [gr-qc].
[25] S. Bernuzzi, T. Dietrich, W. Tichy, and B. Brügmann, Phys.Rev. **D89**, 104021 (2014), arXiv:1311.4443 [gr-qc].
[26] W. Kastaun, F. Galeazzi, D. Alic, L. Rezzolla, and J. A. Font, Phys.Rev. **D88**, 021501 (2013), arXiv:1301.7348 [gr-qc].
[27] P. Tsatsin and P. Marronetti, Phys.Rev. **D88**, 064060 (2013), arXiv:1303.6692 [gr-qc].
[28] W. Kastaun and F. Galeazzi, Phys.Rev. **D91**, 064027 (2015), arXiv:1411.7975 [gr-qc].
[29] W. E. East, V. Paschalidis, F. Pretorius, and S. L. Shapiro, Phys. Rev. **D93**, 024011 (2016), arXiv:1511.01093 [astro-ph.HE].
[30] A. Bauswein, N. Stergioulas, and H.-T. Janka, Eur. Phys. J. A **52**, 56 (2016), arXiv:1508.05493 [astro-ph.HE].
[31] N. Tacik *et al.*, Phys. Rev. **D92**, 124012 (2015), [Erratum: Phys. Rev.D94,no.4,049903(2016)], arXiv:1508.06986 [gr-qc].
[32] D. A. Brown, I. Harry, A. Lundgren, and A. H. Nitz, Phys.Rev. **D86**, 084017 (2012), arXiv:1207.6406 [gr-qc].
[33] M. Agathos, J. Meidam, W. Del Pozzo, T. G. F. Li, M. Tompitak, *et al.*, (2015), arXiv:1503.05405 [gr-qc].
[34] W. Tichy, Phys.Rev. **D74**, 084005 (2006), arXiv:gr-qc/0609087 [gr-qc].
[35] W. Tichy, Class.Quant.Grav. **26**, 175018 (2009), arXiv:0908.0620 [gr-qc].
[36] W. Tichy, Phys.Rev. **D80**, 104034 (2009), arXiv:0911.0973 [gr-qc].
[37] J. Wilson and G. Mathews, Phys.Rev.Lett. **75**, 4161 (1995).
[38] J. Wilson, G. Mathews, and P. Marronetti, Phys.Rev. **D54**, 1317 (1996), arXiv:gr-qc/9601017 [gr-qc].
[39] J. York, James W., Phys.Rev.Lett. **82**, 1350 (1999), arXiv:gr-qc/9810051 [gr-qc].
[40] M. Thierfelder, S. Bernuzzi, and B. Brügmann, Phys.Rev. **D84**, 044012 (2011), arXiv:1104.4751 [gr-qc].
[41] B. Brügmann, J. A. Gonzalez, M. Hannam, S. Husa, U. Sperhake, *et al.*, Phys.Rev. **D77**, 024027 (2008), arXiv:gr-qc/0610128 [gr-qc].
[42] T. Dietrich, S. Bernuzzi, M. Ujevic, and B. Brügmann, Phys. Rev. **D91**, 124041 (2015), arXiv:1504.01266 [gr-qc].
[43] S. Bernuzzi and D. Hilditch, Phys. Rev. **D81**, 084003 (2010), arXiv:0912.2920 [gr-qc].
[44] D. Hilditch, S. Bernuzzi, M. Thierfelder, Z. Cao, W. Tichy, *et al.*, Phys. Rev. **D88**, 084057 (2013), arXiv:1212.2901 [gr-qc].
[45] C. Bona, J. Massó, J. Stela, and E. Seidel, in *The Seventh Marcel Grossmann Meeting: On Recent Developments in Theoretical and Experimental General Relativity, Gravitation, and Relativistic Field Theories*, edited by R. T. Jantzen, G. M. Keiser, and R. Ruffini (World Scientific, Singapore, 1996).
[46] M. Alcubierre, B. Brügmann, P. Diener, M. Koppitz, D. Pollney, *et al.*, Phys.Rev. **D67**, 084023 (2003), arXiv:gr-qc/0206072 [gr-qc].
[47] J. R. van Meter, J. G. Baker, M. Koppitz, and D.-I. Choi, Phys. Rev. **D73**, 124011 (2006), arXiv:gr-qc/0605030.
[48] J. S. Read, B. D. Lackey, B. J. Owen, and J. L. Friedman, Phys. Rev. **D79**, 124032 (2009), arXiv:0812.2163 [astro-ph].
[49] M. Shibata, K. Taniguchi, and K. Uryu, Phys. Rev. **D71**, 084021 (2005), arXiv:gr-qc/0503119.
[50] A. Bauswein, H.-T. Janka, and R. Oechslin, Phys.Rev. **D82**, 084043 (2010), arXiv:1006.3315 [astro-ph.SR].
[51] M. J. Berger and J. Oliger, J.Comput.Phys. **53**, 484 (1984).
[52] M. J. Berger and P. Colella, Journal of Computational Physics **82**, 64 (1989).
[53] W. E. East, F. Pretorius, and B. C. Stephens, Phys.Rev. **D85**, 124010 (2012), arXiv:1112.3094 [gr-qc].
[54] T. Dietrich and S. Bernuzzi, Phys.Rev. **D91**, 044039 (2015), arXiv:1412.5499 [gr-qc].
[55] C. Ronchi, R. Iacono, and P. Paolucci, Journal of Computational Physics **124**, 93 (1996).
[56] J. Thornburg, Class. Quant. Grav. **21**, 3665 (2004), arXiv:gr-qc/0404059 [gr-qc].
[57] D. Pollney, C. Reisswig, E. Schnetter, N. Dorband, and P. Diener, Phys. Rev. **D83**, 044045 (2011), arXiv:0910.3803 [gr-qc].
[58] W. Kastaun, R. Ciolfi, A. Endrizzi, and B. Giaccomazzo, in prep. (2016).
[59] P. Ajith, M. Hannam, S. Husa, Y. Chen, B. Brügmann, *et al.*, Phys.Rev.Lett. **106**, 241101 (2011), arXiv:0909.2867 [gr-qc].
[60] B. P. Abbott *et al.* (Virgo, LIGO Scientific), (2016), arXiv:1606.04856 [gr-qc].
[61] S. Bernuzzi, A. Nagar, S. Balmelli, T. Dietrich, and M. Ujevic, Phys.Rev.Lett. **112**, 201101 (2014), arXiv:1402.6244 [gr-qc].
[62] S. Bernuzzi, T. Dietrich, and A. Nagar, Phys. Rev. Lett. **115**, 091101 (2015), arXiv:1504.01764 [gr-qc].
[63] T. Damour and A. Nagar, Phys. Rev. **D80**, 084035 (2009), arXiv:0906.0096 [gr-qc].
[64] S. Bernuzzi, M. Thierfelder, and B. Brügmann, Phys.Rev. **D85**, 104030 (2012), arXiv:1109.3611 [gr-qc].
[65] S. Bernuzzi and T. Dietrich, Phys. Rev. **D94**, 064062 (2016), arXiv:1604.07999 [gr-qc].
[66] T. Damour, Phys. Rev. **D64**, 124013 (2001), arXiv:gr-qc/0103018.
[67] M. Campanelli, C. Lousto, and Y. Zlochower, Phys.Rev. **D74**, 041501 (2006), arXiv:gr-qc/0604012 [gr-qc].
[68] G. Lovelace, M. Scheel, and B. Szilagyi, Phys.Rev. **D83**, 024010 (2011), arXiv:1010.2777 [gr-qc].
[69] M. A. Scheel, M. Giesler, D. A. Hemberger, G. Lovelace, K. Kuper, M. Boyle, B. Szilgyi, and L. E. Kidder, Class. Quant. Grav. **32**, 105009 (2015), arXiv:1412.1803 [gr-qc].

[70] S. Ossokine, M. Boyle, L. E. Kidder, H. P. Pfeiffer, M. A. Scheel, and B. Szilgyi, Phys. Rev. **D92**, 104028 (2015), arXiv:1502.01747 [gr-qc].

[71] A. Nagar, T. Damour, C. Reisswig, and D. Pollney, Phys. Rev. **D93**, 044046 (2016), arXiv:1506.08457 [gr-qc].

[72] T. Damour, A. Nagar, D. Pollney, and C. Reisswig, Phys.Rev.Lett. **108**, 131101 (2012), arXiv:1110.2938 [gr-qc].

[73] M. Levi and J. Steinhoff, JCAP **1412**, 003 (2014), arXiv:1408.5762 [gr-qc].

[74] SpEC - Spectral Einstein Code, `http://www.black-holes.org/SpEC.html`.

[75] J. Blackman, S. E. Field, C. R. Galley, B. Szilgyi, M. A. Scheel, M. Tiglio, and D. A. Hemberger, Phys. Rev. Lett. **115**, 121102 (2015), arXiv:1502.07758 [gr-qc].

[76] W. E. East, V. Paschalidis, and F. Pretorius, Astrophys. J. **807**, L3 (2015), arXiv:1503.07171 [astro-ph.HE].

[77] S. Bernuzzi, A. Nagar, T. Dietrich, and T. Damour, Phys.Rev.Lett. **114**, 161103 (2015), arXiv:1412.4553 [gr-qc].

[78] T. Damour, A. Nagar, and L. Villain, Phys.Rev. **D85**, 123007 (2012), arXiv:1203.4352 [gr-qc].

[79] S. Bernuzzi, D. Radice, C. D. Ott, L. F. Roberts, P. Moesta, and F. Galeazzi, Phys. Rev. **D94**, 024023 (2016), arXiv:1512.06397 [gr-qc].

[80] K. Takami, L. Rezzolla, and L. Baiotti, Phys.Rev. **D91**, 064001 (2015), arXiv:1412.3240 [gr-qc].

[81] L. Rezzolla and K. Takami, (2016), arXiv:1604.00246 [gr-qc].

[82] A. Bauswein and N. Stergioulas, Phys. Rev. **D91**, 124056 (2015), arXiv:1502.03176 [astro-ph.SR].

[83] J. A. Clark, A. Bauswein, N. Stergioulas, and D. Shoemaker, Class. Quant. Grav. **33**, 085003 (2016), arXiv:1509.08522 [astro-ph.HE].

[84] D. Grossman, O. Korobkin, S. Rosswog, and T. Piran, Mon. Not. Roy. Astron. Soc. **439**, 757 (2014), arXiv:1307.2943 [astro-ph.HE].

[85] K. Kawaguchi, K. Kyutoku, M. Shibata, and M. Tanaka, Astrophys. J. **825**, 52 (2016), arXiv:1601.07711 [astro-ph.HE].

[86] T. Dietrich *et al.*, In preparation (2016).

[87] E. Poisson, Phys. Rev. **D57**, 5287 (1998), arXiv:gr-qc/9709032 [gr-qc].

[88] M. Levi and J. Steinhoff, JCAP **1601**, 011 (2016), arXiv:1506.05056 [gr-qc].

[89] M. Levi and J. Steinhoff, (2016), arXiv:1607.04252 [gr-qc].

[90] T. Damour, B. R. Iyer, and B. Sathyaprakash, Phys.Rev. **D62**, 084036 (2000), arXiv:gr-qc/0001023 [gr-qc].